Engineering 41 (2024) 84–92

Contents lists available at ScienceDirect

Engineering

journal homepage: www.elsevier.com/locate/eng

Research
Green Chemical Engineering—Article

Direct Ethylene Purification from Cracking Gas via a Metal–Organic Framework Through Pore Geometry Fitting

Yang Chen [a,#], Zhenduo Wu [b,f,#], Longlong Fan [c,#], Rajamani Krishna [d], Hongliang Huang [e], Yi Wang [a], Qizhao Xiong [a], Jinping Li [a,*], Libo Li [a,*]

[a] College of Chemical Engineering and Technology, Taiyuan University of Technology, Taiyuan 030024, China
[b] City University of Hong Kong (Dongguan), Dongguan 523000, China
[c] Institute of High Energy Physics, Chinese Academy of Sciences, Beijing 100049, China
[d] Van't Hoff Institute for Molecular Sciences, University of Amsterdam, Amsterdam 1098 XH, Netherlands
[e] State Key Laboratory of Separation Membranes and Membrane Processes, Tiangong University, Tianjin 300387, China
[f] Center for Neutron Scattering, City University of Hong Kong Shenzhen Research Institute, Shenzhen 518057, China

ARTICLE INFO

Article history:
Received 8 August 2023
Revised 23 January 2024
Accepted 24 January 2024
Available online 13 March 2024

Keywords:
Metal–organic frameworks
Pore regulation
Adsorptive separation
One-step purification
C_2H_4 purification

ABSTRACT

The direct one-step separation of polymer-grade C_2H_4 from complex light hydrocarbon mixtures has high industrial significance but is very challenging. Herein, an ethylene-adsorption-weakening strategy is applied for precise regulation of the pore geometry of four tailor-made metal–organic frameworks (MOFs) with pillar-layered structures, dubbed TYUT-10/11/12/13. Based on its pore geometry design and functional group regulation, TYUT-12 exhibits exceptional selective adsorption selectivity toward C_3H_8, C_3H_6, C_2H_6, C_2H_2, and CO_2 over C_2H_4; its C_2H_6/C_2H_4 adsorption selectivity reaches 4.56, surpassing the record value of 4.4 by $Fe_2(O_2)$(dobdc) (dobdc^{4-} = 2,5-dioxido-1,4-benzenedicarboxylate). The weak π–π stacking binding affinity toward C_2H_4 in TYUT-12 is clearly demonstrated through a combination of neutron powder diffraction measurements and theoretical calculations. Breakthrough experiments demonstrate that C_2H_4 can be directly obtained from binary, ternary, quaternary, and six-component light hydrocarbon mixtures with over 99.95% purity.

1. Introduction

Ethylene (C_2H_4) is a pivotal product in the global chemical industry [1–3]. Catalytic cracking, steam cracking, and other C_2H_4 production processes are often conducted on mixtures containing C_2H_4 along with propane (C_3H_8), propylene (C_3H_6), ethane (C_2H_6), acetylene (C_2H_2), carbon dioxide (CO_2), and other compounds [4–8]. In the traditional separation process, to obtain polymer-grade C_2H_4 from crude C_2H_4, an amine solution must be employed to absorb and thus remove CO_2, a selective catalytic hydrogenation must be implemented to purify alkynes, and multiple stages of cryogenic distillation must be carried out; however, this process is very energy intensive, and its input costs are high (Fig. 1) [9–11]. Because they can be conducted at ambient temperature using efficient and flexible devices, physisorption-centered separation processes hold the potential to significantly curtail energy consumption in gas separation [12–16]; thus, these processes are expected to partially replace traditional energy-intensive C_2H_4 separation technologies. The appeal of adsorption separation technology lies in the breakthrough innovations that have been achieved in the field of adsorbents. The limits of commercial adsorbents (e.g., zeolite, activated carbon, silica gel, and alumina) have already been recognized: namely, poor adsorption capacity and poor selectivity for hydrocarbon mixtures due to the scarcity of adsorption sites and an insufficient recognition mechanism, especially for the isolation of hydrocarbons from multi-component mixtures containing mutually similar hydrocarbons (Fig. S1 in Appendix A) [17–22]. As a means of addressing the challenges in these industrially important hydrocarbon-separation processes, metal–organic frameworks (MOFs) have provided good opportunities and platforms in the realm of gas separation owing to their porosity and diversity [23,24]. Over the past ten years, a relatively complete structural design method based on MOF topology has been developed, along with a functional group surface cooperative regulation strategy [25–27].

Research focusing on the MOF-based direct separation of C_2H_4 from binary mixtures (i.e., C_2H_4/C_2H_6, C_2H_4/C_2H_2, C_3H_8/C_3H_6, and

* Corresponding authors.
E-mail addresses: jpli211@hotmail.com (J. Li), lilibo@tyut.edu.cn (L. Li).
# These authors contributed equally to this work.

https://doi.org/10.1016/j.eng.2024.01.024

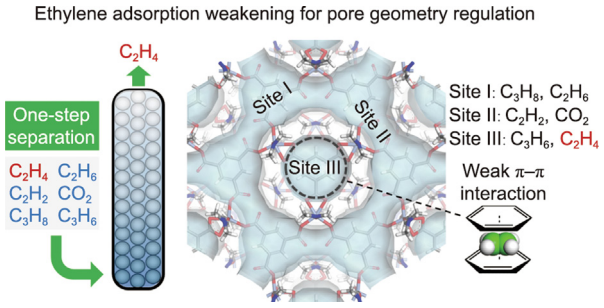

Fig. 1. Schematic diagram of the ethylene-adsorption-weakening strategy for one-step ethylene purification via a single MOF adsorbent.

C_2H_2/CO_2) over the past ten years [1,4,8,12–14,26], ternary mixtures (i.e., $C_2H_4/C_2H_6/C_2H_2$ and $C_2H_4/C_2H_2/CO_2$) over the past five years [5–7,15,19,28–31], and quaternary mixtures (i.e., $C_2H_6/C_2H_4/C_2H_2/CO_2$) over the past three years [32–35] has produced continuous breakthroughs. Notably, as the studied mixtures get closer in composition to the actual industrial gas, the separation becomes more difficult, and the observed adsorption selectivity (especially between C_2H_6 and C_2H_4) and separation performance of the reported adsorbents decrease significantly. Indeed, the key stumbling block that limits the C_2H_4 separation efficiency of multi-component mixtures is generally the ineffective purification of C_2H_4 from C_2H_6. Li et al. [14] and Lin et al. [36] reported the achievement of ethylene purification from binary C_2H_6/C_2H_4 mixtures using the top-performing C_2H_6-selective adsorbents $Fe_2(O_2)(dobdc)$ ($dobdc^{4-}$ = 2,5-dioxido-1,4-benzenedicarboxylate) and $Cu(Qc)_2$ (HQc = quinoline-5-carboxylic acid), which demonstrated notable C_2H_6/C_2H_4 selectivities of 4.4 and 3.4, respectively. Subsequently, Gu et al. [7] reported the introduction of Lewis basic sites into UiO-67 (UiO: Universitetet i Oslo) for the direct purification of ethylene from ternary mixtures; however, the materials were reported to afford C_2H_6/C_2H_4 selectivities of only 1.49 and 1.7, respectively. Chen et al. [32] integrated three kinds of MOFs characterized by different selectivities into a fixed bed for the direct production of polymer-grade ethylene from ternary and quaternary mixtures; notably, the C_2H_6/C_2H_4 selectivity was decreased to 1.7. Recently, Wu et al. [31] proposed a robust Al-MOF (Al-PyDC, H_2PyDC = 2,5-pyrroledicarboxylate) with multiple supramolecular binding sites for highly efficient one-step C_2H_4 purification from ternary mixtures, although its C_2H_6/C_2H_4 selectivity only reached 1.9. With the ultimate goal of simplifying the C_2H_4 separation process, reducing its cost and energy consumption, and creating an efficient adsorbent that affords the one-step purification of ethylene from multi-component refinery gas, the key target of the present study was to weaken the adsorption of C_2H_4 in comparison with other refinery gas molecules (i.e., C_3H_8, C_3H_6, C_2H_6, C_2H_2, and CO_2). The approach adopted herein is obviously different from the traditional strategy utilized to design efficient adsorbents [37,38].

In order to weaken C_2H_4 adsorption through pore geometry design, four kinds of pillar-layered MOFs were systematically constructed: Ni(BTC)(pyrazine) [39], $Ni(BTC)(pyridine)_{0.67}(H_2O)_{1.33}$, $Ni(BTC)(DMF)_2$ [40], and $Co(BTC)(DMF)_2$, which were dubbed TYUT-10, TYUT-11, TYUT-12, and TYUT-13, respectively (TYUT: Taiyuan University of Technology; BTC: trimesic acid; DMF: *N*,*N*′-dimethylformamide; see Figs. S2–S9 and Tables S1 and S2 in Appendix A). Through the precise regulation of interlayer pore segmentation, we obtained suitable segmented channels between layers in TYUT-12 that are decorated with functional groups. In fact, the abundance of methyl groups, carboxylate oxygens, and nitrogen atoms in the interlayer ring-mounted channels results in a strong recognition ability for C_3H_8, C_3H_6, C_2H_6, C_2H_2, and CO_2 molecules that relies on C–H···O, C–H···N, and C–H···π interactions; however, the C_2H_4 molecule is mainly recognized in flat pores through relatively weak π···π interactions. As a result of its unique pore system, TYUT-12 does not just demonstrate exceptional C_2H_6/C_2H_4 adsorption selectivity (4.56); its use also permits—for the first time—the direct production of high-purity C_2H_4 (> 99.95%) from six-component refinery gas mixtures ($C_3H_8/C_3H_6/C_2H_6/C_2H_4/C_2H_2/CO_2$) through a single breakthrough operation conducted under ambient conditions, thus demonstrating the great potential of this MOF for realizing this challenging C_2H_4 separation process.

2. Materials and methods

2.1. Preparation of samples

(1) Synthesis of Ni(BTC)(pyrazine) (TYUT-10): The creation of the single-crystal sample was conducted using a method previously described, incorporating slight adjustments [39].

(2) Synthesis of $Ni(BTC)(pyridine)_{0.67}(H_2O)_{1.33}$ (TYUT-11): A mixture containing $Ni(NO_3)_2{\cdot}6H_2O$ (0.029 g, 0.1 mmol), H_3BTC (0.021 g, 0.1 mmol), and pyridine (81 μL, 1.0 mmol) was dissolved in 10 mL of DMF, sealed within a 20 mL scintillation vial, and subjected to a 373 K reaction for 48 h. Subsequently, the mixture was slowly cooled to ambient temperature. Upon reaching room temperature, the supernatant was discarded, and the residue was washed with DMF three times. The resulting material was then air-dried at room temperature to obtain green crystal samples (yield: 0.0176 g, 51.2% based on the BTC ligand; elemental analysis calculated (%) for $Ni_{1.5}C_{18.5}H_{9.5}NO_{11}$: C 43.62, H 1.91, N 2.68; found (%): C 43.53, H 1.86, N 2.75).

(3) Synthesis of $Ni(BTC)(DMF)_2$ (TYUT-12): The conventional preparation method used for the single-crystal sample was in accordance with a previous reported method [40]. A 10 g level synthesis method was developed as follows: $Ni(NO_3)_2{\cdot}6H_2O$ (8.70 g, 0.03 mol) and H_3BTC (6.30 g, 0.03 mol) were dissolved in 300 mL of DMF, transferred into a 500 mL round bottom flask, and refluxed at 393 K for 15 h. After the reaction concluded, the solvent was cooled to room temperature. The resultant green block crystals were gathered, subjected to three washes with DMF, and subsequently air dried (yield: 11.47 g, 92.5% based on the BTC ligand). The abovementioned reacted solvent can be recovered and reused more than five times.

(4) Synthesis of $Ni(BTC)(DMF\text{-}D_7)_2$ (TYUT-12-D_7): For the neutron powder diffraction (NPD) experiments, deuterated DMF (DMF-D_7) was used to prepare TYUT-12-D_7 in order to reduce the influence of the hydrogen (H) element on the test. The preparation method was as follows: A combination of H_3BTC (0.105 g, 0.5 mmol) and $Ni(NO_3)_2{\cdot}6H_2O$ (0.145 g, 0.5 mmol) was dissolved in 5 mL of deuterated DMF-D_7. This mixture was sealed within a 20 mL small vial and subjected to a 393 K reaction for 2 d, followed by a gradual cooldown to room temperature. Once the temperature reached ambient levels, the supernatant was discarded, and the obtained crystals were washed three times with DMF-D_7. The crystals were then allowed to air dry at room temperature (yield: 0.172 g, 80.75%). The solution (DMF-D_7) after the above reaction can be recycled and used three times, and the TYUT-12-D_7 product can be obtained by adding 80% of the basic raw materials each time (Fig. S10 in Appendix A).

(5) Synthesis of $Co(BTC)(DMF)_2$ (TYUT-13): A blend of $Co(NO_3)_2.6H_2O$ (0.146 g, 0.5 mmol) and H_3BTC (0.105 g, 0.5 mmol) was dissolved in 10 mL of DMF and enclosed within a 23 mL Teflon-lined autoclave. The mixture was subjected to a reaction at 393 K for 48 h, then gradually cooled down to room temperature. The prepared crystals were washed three times with DMF. The crystals were then allowed to air dry at room temperature,

resulting in the acquisition of purple crystal samples (yield: 0.168 g, 81.6% based on the BTC ligand; elemental analysis calculated (%) for $Co_3C_{45}H_{51}N_6O_{24}$: C 43.75, H 4.23, N 6.77; found (%): C 43.69, H 4.13, N 6.80).

2.2. Single-crystal X-ray diffraction and NPD

Crystallographic data acquisition was conducted using a Bruker D8 VENTURE PHOTON II area-detector diffractometer (Bruker AXS GmbH, Germany), employing graphite-monochromated Ga Kα radiation with a wavelength (λ) of 1.34139 Å (1 Å = 10^{-10} m) for TYUT-11 and Mo Kα radiation (λ = 0.71073 Å) for TYUT-13 using the ω-scan technique. The SAINT program [41] was used for the integration of diffraction data and the intensity correction for the Lorentz and polarization effects. Semi-empirical absorption corrections were applied using the SADABS program [42]. The structures were solved using direct methods and refined with the full-matrix least-squares technique based on F^2 using the SHELXL-97 program [43]. All non-hydrogen atoms were refined anisotropically, and all the hydrogen atoms were introduced at the calculated positions.

The NPD data were collected using the multi-physics instrument (MPI) at the China Spallation Neutron Source, with a Q range of 1.1–30 $Å^{-1}$ [44,45]. The detectors were calibrated using a National Institute of Standards and Technology (NIST) silicon powder standard prior to the measurements. The C_2D_4-loaded powder sample with a mass of about 3 g was loaded in a vanadium can at room temperature. NPD data were acquired at a temperature of 10 K under vacuum for 3 h. Deuterated gas, C_2D_4, was used to reduce the large incoherent neutron scattering produced by the H atoms. The empty vanadium can and background data were obtained for data reduction and correction using the program Mantid. A Rietveld analysis was performed using GSAS-II. Herein, a $P1$ phase model was employed for the structural refinement. In order to obtain a reliable and stable refinement result, the bonds in the C_2D_4, deuterated DMF-D_7, and 1,3,5-benzenetricarboxylic acid were constrained by rigid-body models to reduce the number of parameters. An isotropic thermal motion model was used for rigid bodies with the same type.

The crystallographic data is synopsized in Tables S1 and S2. The X-ray crystallographic data and NPD data related to TYUT-11, TYUT-12·0.72C_2D_4, and TYUT-13 have been deposited at the Cambridge Crystallographic Data Centre (CCDC), under the deposition numbers 2110177, 2246837, and 2115139, respectively.

2.3. Adsorption and breakthrough experiments

Adsorption and desorption isotherms were acquired using an Intelligent Gravimetric Analyzer (IGA-001, Hiden Isochema, UK; detection limit of 0.1 μg based on an ultra-high-precision microbalance). All samples were CH_2Cl_2-exchanged over three times in 2 d, and were then activated under high vacuum (0.1 Pa) at 373 K for 12 h. Adsorption equilibrium data was gathered after maintaining the weight for a minimum of 30 min to achieve adsorption equilibrium at each predetermined pressure point on the isotherm. In each adsorption test, the mass of the preactivated materials was approximately 80 mg. To obtain kinetic adsorption data at 298 K, the mass of the sample was collected in real time after increasing the pressure from 0.1 Pa to 100 kPa (20 kPa·min^{-1}) and was then maintained at 100 kPa for over 60 min.

Dynamic separation experiments for the C_2H_6/C_2H_4, C_2H_2/C_2H_4, CO_2/C_2H_4, $C_2H_6/C_2H_4/C_2H_2$, $C_2H_6/C_2H_4/C_2H_2/CO_2$, and $C_3H_8/C_3H_6/C_2H_6/C_2H_4/C_2H_2/CO_2$ mixtures were conducted with a flow rate of 2 mL·min^{-1} (298 K, 100 kPa). For this experimentation, 1.50 g of TYUT-12 with a particle size of approximately 50 μm was loaded into a stainless steel column with the dimensions ϕ4 mm × 120 mm. Subsequently, the sample was activated by vacuum at 393 K for a duration of 12 h. The reaction vessels were positioned within a temperature-controlled environment, maintaining a temperature of 298 K. Mass flow controllers were employed to regulate the flow rates, while the gas stream effluent from the adsorption bed was detected using an Agilent 490 gas chromatograph (Agilent Technologies, USA). Before this experiment, the materials were activated by purging the column with helium (He) gas for a duration of 1 h at 393 K. The desorption experiments were conducted under helium flow (10 mL·min^{-1}) at room temperature for C_2H_6/C_2H_4 and at 333 K for C_2H_2-containing mixtures. An ABR automated breakthrough analyzer (Hiden Isochema, UK) was used to conduct single-component breakthrough experiments for TYUT-12 at a temperature of 298 K and a pressure of 100 kPa. The ABR automated breakthrough analyzer was also employed to perform quaternary mixture breakthrough experiments for TYUT-12 at 298 K and a pressure of 300 kPa.

3. Results and discussion

The series of pillar-layered MOFs was constructed using metallic nickel (Ni) or cobalt (Co), BTC, and the "pillar" compounds (pyrazine, pyridine, or DMF; Fig. 2). The obtained materials are composed of graphene-like layers, where the repeating unit, which extends in every direction, consists of three metal ions and a molecule of BTC, forming a hexagon-like hole. The role of the pillars is to connect or support the layers, so that porous channels are formed between them. In the case of TYUT-10, a three-dimensional (3D) structure, with 3D channels extending in all directions, is formed as a result of the pillar, the bidentate ligand pyrazine, connecting the graphene-like layers that compose the material. In contrast, by replacing pyrazine with the monodentate ligand pyridine, the pillar can only play a supporting role for the layers, so that TYUT-11, a two-dimensional (2D) MOF with staggered layers, is produced. From the perspective of the structural and channel differences illustrated in Figs. 2 and S2, the formation of the layers causes the 3D channels in TYUT-10 to be segmented into each layer, which can result in blocking the gas diffusion between different layers, thus enhancing the system's ability to discriminate between different gases. Notably, the abundant porosity and high specific surface area of TYUT-10 result in a very high adsorption capacity (~4 mmol·g^{-1}) for C_2H_6 and C_2H_4 but a low C_2H_6/C_2H_4 selectivity (1.37). Given the separation of pores located in different layers, C_2H_6 and C_2H_4 can only diffuse within layers, while diffusion between different layers is prevented. The resulting confinement effect causes the C_2H_6/C_2H_4 selectivity in TYUT-11 to increase to 1.55 with respect to TYUT-10 (Figs. S11 and S12 and Tables S3–S5 in Appendix A).

In order to enhance the ability to selectively adsorb C_2H_6, DMF molecules were utilized as pillars in the construction of pillar-layered MOFs with increased C_2H_6 binding affinity resulting from multiple van der Waals interactions; the MOFs obtained in this way were dubbed TYUT-12 (metal: Ni) and TYUT-13 (metal: Co). In comparison with the porous TYUT-10, the 2D TYUT-12, in which the DMF pillars act as layer supports, comprises interlayer channels that are completely segmented by the staggered layers. Connected hexagonal channels are formed between layers, at the center of which are independent oblate spherical cavities. Through the interlayer restriction and pore adjustment in the structure of TYUT-12, as well as the introduction of methyl groups, carbonyl oxygens, and nitrogen (N) atoms (resulting from the addition of DMF), the adsorption selectivity of TYUT-12 toward gaseous C_3H_8, C_3H_6, C_2H_6, C_2H_2, and CO_2 over C_2H_4 is enhanced. As shown by the adsorption curves of TYUT-12, this MOF's adsorption capacity and affinity for C_3H_8, C_3H_6, C_2H_6, C_2H_2, and CO_2 are significantly stronger than those for C_2H_4. In particular, the difference in

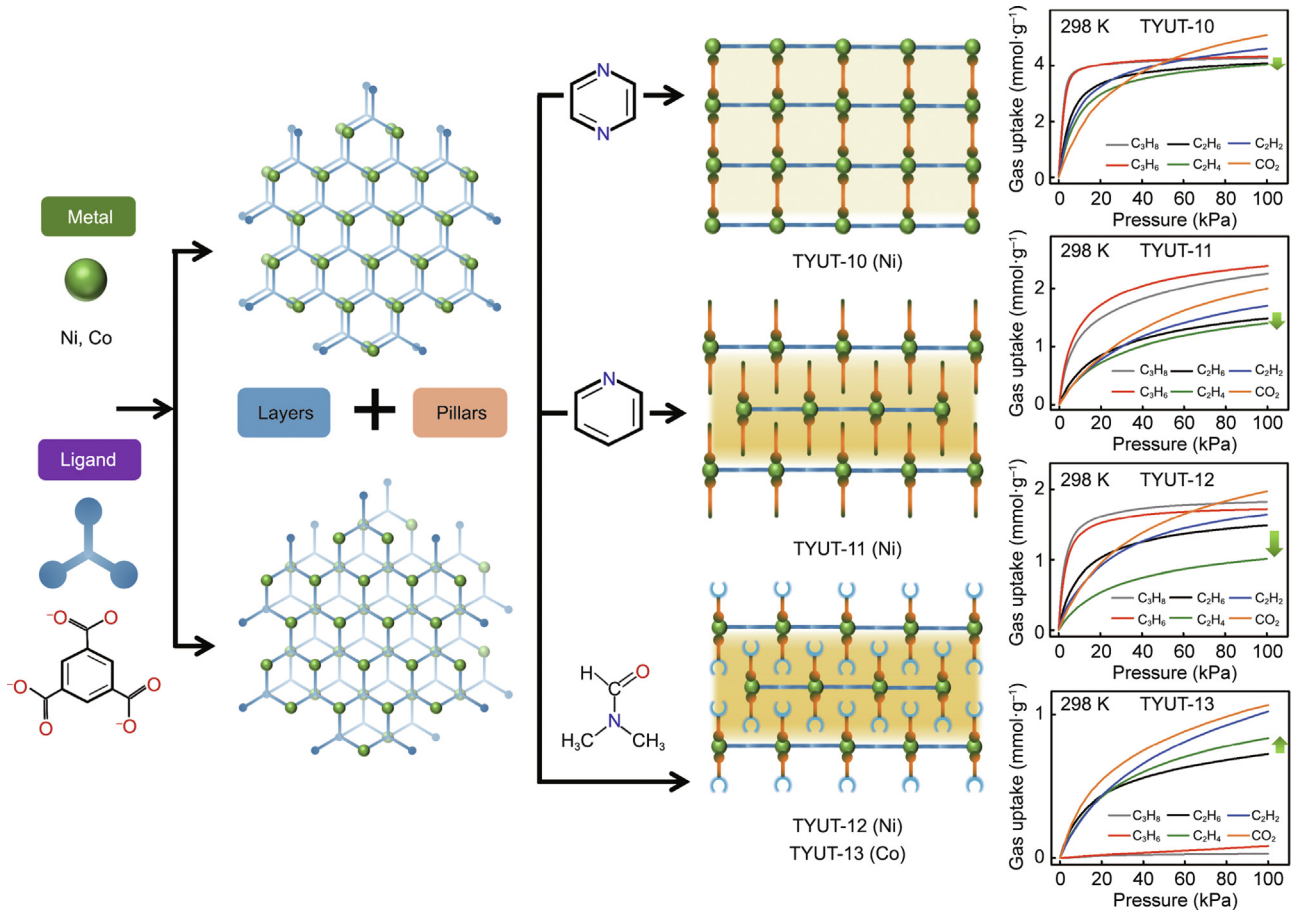

Fig. 2. Structural design and gas adsorption properties. Schematic diagram of the structural regulation of various pillar-layered MOFs and the said MOFs' C_3H_8, C_3H_6, C_2H_6, C_2H_4, C_2H_2, and CO_2 adsorption isotherms.

adsorption between C_2H_6 and C_2H_4 is significantly enhanced with respect to TYUT-10 and TYUT-11. In contrast, due to the difference in the coordinating abilities of Co and Ni, the coordinated DMF in TYUT-13 has a weaker interaction with Co, while its hydrogen bond with the carboxylate oxygens from the above layers is stronger, leading to structural distortion and interlayer distance reduction (Figs. 3 and S9). As a result, this MOF's capacity for the adsorption of the mentioned gaseous molecules is drastically reduced. Through the tailor-made interlayer pore segmentation control in TYUT-12, in the optimized interlayer confinement channels, the adjustment of the specific adsorption sites of the benzene ring sandwich with weak π···π interactions achieves the goal of weakening ethylene adsorption. This material was thus ultimately selected as the best candidate for the direct purification of C_2H_4 from multi-component refinery gas mixtures (C_3H_8/C_3H_6/C_2H_6/C_2H_4/C_2H_2/CO_2).

The adsorption of gaseous light hydrocarbons on TYUT-12 at different temperatures (273, 288, and 298 K) was investigated in detail; according to the relevant results, over a wide temperature range, the adsorption capacities for C_3H_8, C_3H_6, C_2H_6, C_2H_2, and CO_2 were significantly higher than that for C_2H_4 (Figs. 3(a) and (b) and Figs. S13–S15 in Appendix A). Especially under low pressure (< 10 kPa), the uptake of C_2H_6 by TYUT-12 was higher than the uptakes of C_2H_4, C_2H_2, and CO_2, indicating that TYUT-12's interlayer channels and functional groups effectively provide rich and strong binding sites for C_2H_6 molecules. In the case of large gas adsorption differences, as shown in Figs. 3(c) and (d), TYUT-12 exhibited outstanding equimolar C_2H_6/C_2H_4 adsorption selectivities at 100 kPa (4.56 at 298 K and 7.20 at 273 K) and a high C_2H_6/C_2H_4 adsorption ratio at 10 kPa (2.21 at 298 K and 1.80 at 273 K)—values that are generally higher than those of the top-performing MOFs reported in the literature (Fig. 3(e) and Fig. S16 in Appendix A) [46]. Moreover, the equimolar C_3H_8/C_2H_4, C_3H_6/C_2H_4, C_2H_2/C_2H_4, and CO_2/C_2H_4 adsorption selectivities afforded by TYUT-12 were determined to be in the 3.2–41 range at 298 and 273 K. Even for the gas adsorption selectivity of a 1:99 gas composition (all the compositions of gas mixtures are volume ratio unless otherwise specified), TYUT-12 exhibited good performance (Fig. S17 in Appendix A). Its excellent adsorption selectivities for C_3H_8, C_3H_6, C_2H_6, C_2H_2, and CO_2 with respect to C_2H_4 point to the great potential of TYUT-12 for the efficient purification of C_2H_4 from multi-component mixtures.

During the separation process, gas diffusion is an important limiting factor; therefore, the adsorption kinetics of the gas molecules in TYUT-12 were investigated in detail (Figs. S18, S19, and Table S6 in Appendix A) [47]. The time needed to reach the adsorption equilibrium was similar for C_2H_6, C_2H_4, C_2H_2, and CO_2, while the calculated diffusion coefficients of C_3H_8 and C_3H_6 were significantly smaller than those of C_2H_6 and C_2H_4, indicating the obvious diffusion restriction of larger molecules in the pore channels. The characteristics of the desorption curves also indicate that the time required for C_3H_8 desorption is the longest and the time for C_2H_6 and C_2H_4 desorption is relatively shorter—a trend that is related to molecular size and the interaction with the structures. The values for the isosteric heat of adsorption (Q_{st}) for the processes of C_3H_8, C_3H_6, C_2H_6, C_2H_4, C_2H_2, and CO_2 adsorption on TYUT-12 were calculated using a virial equation based on the adsorption curves obtained at different temperatures (Fig. 3(f) and Figs. S20 and

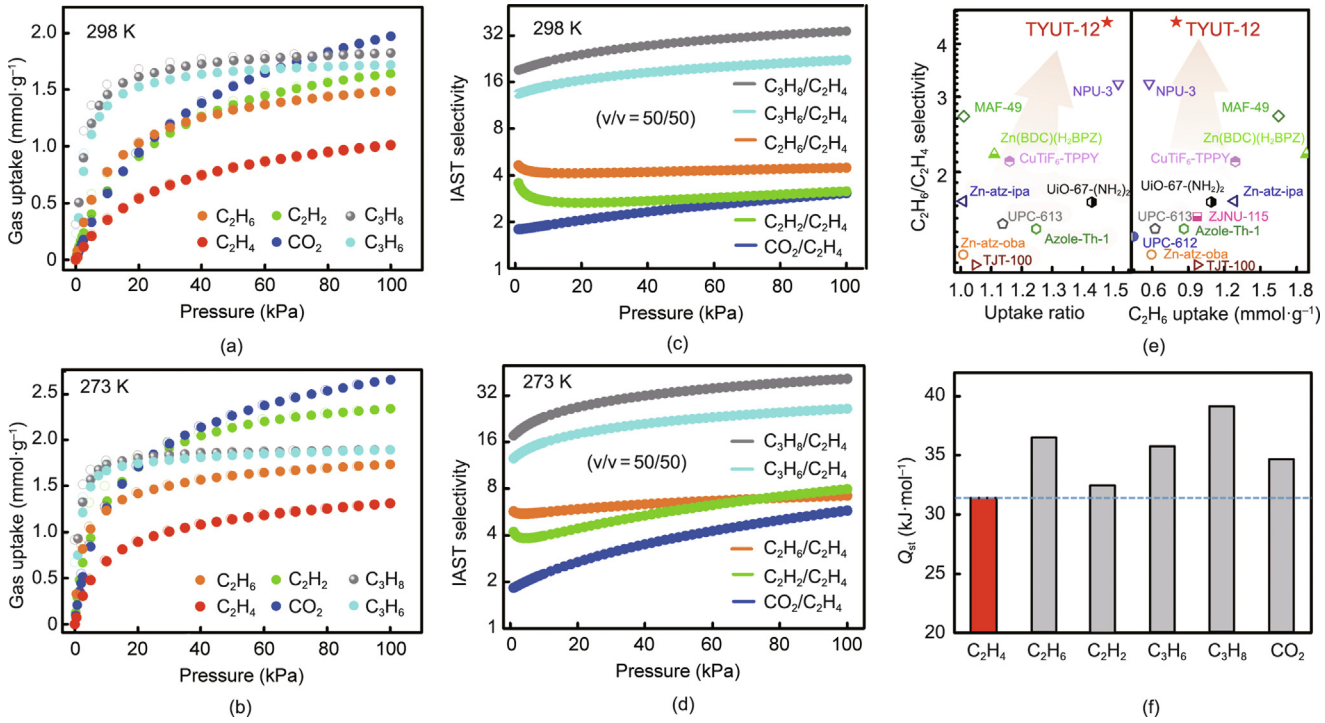

Fig. 3. Data reflecting the adsorption performance of TYUT-12. (a, b) Single-component gas adsorption (solid circles) and desorption (hollow circles) isotherms of C_3H_8, C_3H_6, C_2H_6, C_2H_4, C_2H_2, and CO_2 on TYUT-12 at 298 and 273 K. (c, d) Ideal adsorbed solution theory (IAST) selectivities curves for TYUT-12 at 298 and 273 K. (e) C_2H_6/C_2H_4 IAST selectivities, uptake ratios, and C_2H_6 uptake at 100 kPa of TYUT-12 compared with benchmark C_2H_6-selective MOFs for the separation of multi-component mixtures at 298 K. NPU: Northwestern Polytechnical University; MAF: metal–azolate framework; H_2BDC: 1,4-benzenedicarboxylic acid; H_2BPZ: 3,3′,5,5′-tetramethyl-4,4′-bipyrazole; TPPY: 5,10,15,20-tetra(4-pyridyl)-21*H*,23*H*-porphyrin; atz: 3-amino-1,2,4-triazolate; ipa: isophthalate; H_2oba: 4,4-dicarboxyl diphenyl ether; UPC: China University of Petroleum (East China); ZJNU: Zhejiang Normal University; TJT: Tianjin University of Technology. (f) Values of the isosteric heat of adsorption (Q_{st}) of C_3H_8, C_3H_6, C_2H_6, C_2H_2, CO_2, and C_2H_4 for the process of adsorption on TYUT-12.

S21 in Appendix A). Near zero coverage, the Q_{st} values for the adsorptions of C_3H_8, C_3H_6, C_2H_6, C_2H_4, C_2H_2, and CO_2 on the said MOF were calculated to be 39.2, 35.8, 36.6, 31.4, 32.4 and 34.8 kJ·mol^{-1}, respectively. Notably, the order of the Q_{st} values of the mentioned gases is consistent with their adsorption behavior, as inferred from the results of the single-component gas adsorption experiments (Figs. 3(a) and (b)); the Q_{st} values also point to the unique C_2H_4 adsorption environment of TYUT-12, which results in C_2H_4 exhibiting the weakest binding affinity for the said MOF.

In order to demonstrate the C_2H_4 separation potential of TYUT-12 from gas mixtures, key separation experiments were conducted on the binary mixtures C_2H_6/C_2H_4 (50:50, 10:90, and 5:95), C_2H_2/C_2H_4 (50:50), and CO_2/C_2H_4 (50:50); the ternary mixture $C_2H_6/C_2H_4/C_2H_2$ (9:90:1); the quaternary mixture $C_2H_6/C_2H_4/C_2H_2/CO_2$ (9:89:1:1 and 9:85:1:5); and the six-component mixture $C_3H_8/C_3H_6/C_2H_6/C_2H_4/C_2H_2/CO_2$ (9:9:10:70:1:1) (Fig. 4). As shown in Fig. 4(a), C_2H_4 was efficiently separated from an equimolar C_2H_6/C_2H_4 mixture by passing the said mixture over a fixed bed of TYUT-12 under ambient conditions; using this approach, high-purity C_2H_4 (99.95%) was directly obtained from the outlet over a period of time. The dynamic uptakes of C_2H_6 and C_2H_4 during the separation process were 1.16 and 0.83 mmol·g^{-1}, respectively, which were slightly lower than the static adsorption capacities due to the effect of micropore diffusion. Moreover, in the separation of C_2H_6/C_2H_4 (10:90 and 5:95) (Fig. S22 in Appendix A), higher purity C_2H_4 products with a longer separation time were obtained. Separation experiments were also conducted on the equimolar C_2H_4-containing binary mixtures C_3H_8/C_2H_4, C_3H_6/C_2H_4, C_2H_2/C_2H_4, and CO_2/C_2H_4. As shown by the data reported in Fig. S23 in Appendix A, all the gas mixtures afforded the isolation of high-purity C_2H_4, indicating the potential of TYUT-12 to be used in the separation of C_2H_4 from mixtures containing C_3H_8, C_3H_6, C_2H_6, C_2H_2, and CO_2. In the cases of the ternary mixture $C_2H_6/C_2H_4/C_2H_2$ (9:90:1) and the quaternary mixture $C_2H_6/C_2H_4/C_2H_2/CO_2$ (9:89:1:1 and 9:85:1:5) (Figs. 4(b) and (c) and Figs. S24 and S25 in Appendix A), TYUT-12 also demonstrated a good C_2H_4 separation performance, with high-purity C_2H_4 (99.98%) being obtained. As for the challenging task of carrying out the direct purification of C_2H_4 from six-component refinery gas mixtures ($C_3H_8/C_3H_6/C_2H_6/C_2H_4/C_2H_2/CO_2$, 9:9:10:70:1:1), which has never before been realized, TYUT-12 again afforded a clear and efficient C_2H_4 separation. Based on the unique C_2H_4 binding affinity and locations in TYUT-12, five of the component gases of the mixture (C_3H_8, C_3H_6, C_2H_6, C_2H_2, and CO_2) were adsorbed onto the TYUT-12, while C_2H_4 was eluted from it at first, then quickly reached equilibrium. Correspondingly, C_2H_4 at over 99.96% purity was isolated in one step from the six-component mixture $C_3H_8/C_3H_6/C_2H_6/C_2H_4/C_2H_2/CO_2$ (9:9:10:70:1:1; Fig. 4(d)). The amount of C_2H_4 captured under dynamic conditions in the TYUT-12 was calculated to be 0.90 and 0.86 mmol·g^{-1} in the separation processes conducted on quaternary or six-component mixtures, respectively; thus, about 0.78 and 0.60 mmol·g^{-1} C_2H_4 productivity (> 99.95% purity) can be obtained by one separation process (Fig. 4(e) and Fig. S26 in Appendix A). As shown in Fig. S27 in Appendix A, it is worth mentioning that the material still exhibits good quaternary mixture ($C_2H_6/C_2H_4/C_2H_2/CO_2$, 9:89:1:1) separation under high pressure (300 kPa), and the corresponding C_2H_4 productivity can be increased to 1.27 mmol·g^{-1} (standard temperature and pressure).

Breakthrough repeatability tests demonstrated that TYUT-12 exhibits a stable separation performance and that high-purity C_2H_4 can be continuously obtained from quaternary gas mixtures (Fig. 4(f) and Fig. S28 in Appendix A). Furthermore, the

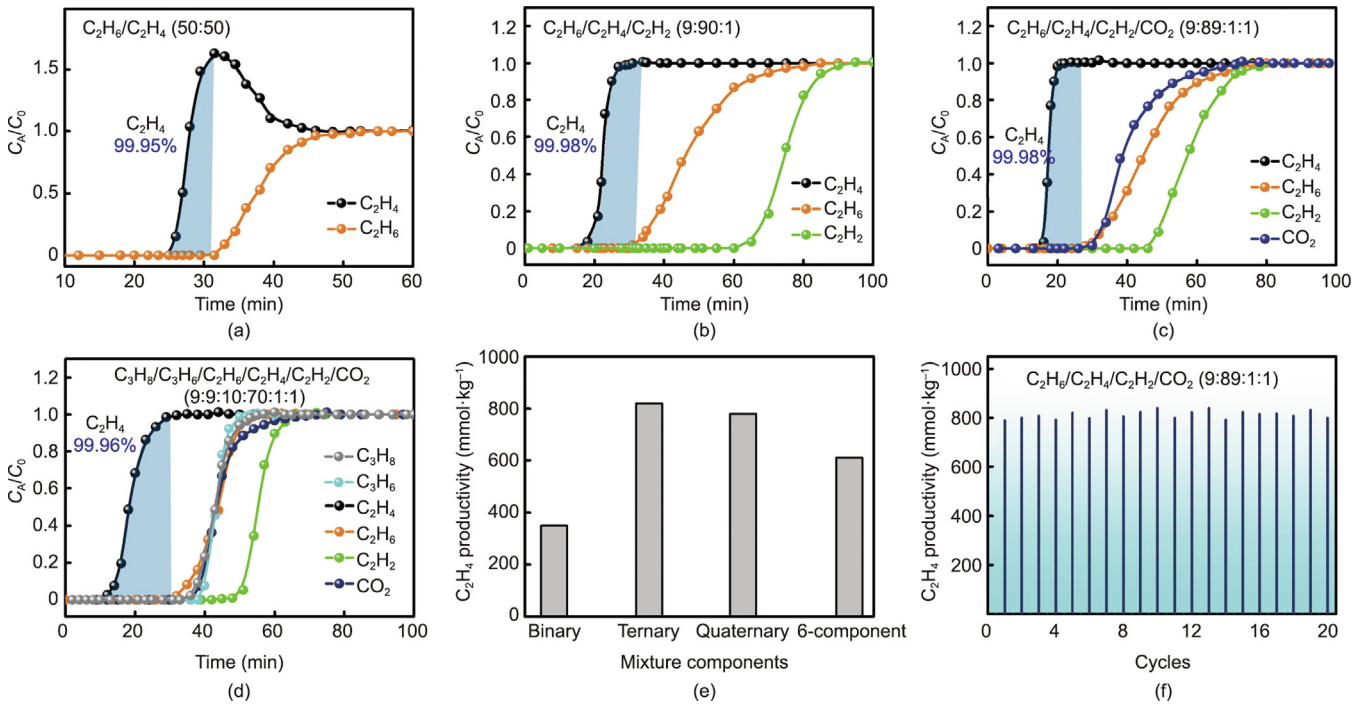

Fig. 4. Data reflecting the C_2H_4 separation performance. Experimental breakthrough curves for different C_2H_4-containing mixtures on TYUT-12 at 298 K and 100 kPa: (a) C_2H_6/C_2H_4 (50:50); (b) $C_2H_6/C_2H_4/C_2H_2$ (9:90:1); (c) $C_2H_6/C_2H_4/C_2H_2/CO_2$ (9:89:1:1); and (d) $C_3H_8/C_3H_6/C_2H_6/C_2H_4/C_2H_2/CO_2$ (9:9:10:70:1:1). (e) Polymer-grade C_2H_4 (> 99.95%) productivity recorded for different C_2H_4-containing mixtures. (f) Polymer-grade C_2H_4 (> 99.95%) productivity recorded over 20 consecutive separation cycles of $C_2H_6/C_2H_4/C_2H_2/CO_2$ (9:89:1:1) conducted on TYUT-12 at 298 K. C_A is the outlet gas concentration, and C_0 is the outlet gas concentration at equilibrium.

breakthrough and regeneration curves of single-component C_3H_8, C_3H_6, C_2H_6, C_2H_4, C_2H_2, and CO_2 gases on TYUT-12 confirmed that, under dynamic conditions, these gases can be easily desorbed from TYUT-12 by vacuuming (Figs. S29–S34 in Appendix A). The results of the dynamic separation experiments conducted on binary to six-component mixtures thus verified the ability of TYUT-12 to afford the isolation of high-purity C_2H_4 (> 99.95%) from different mixtures in one step, indicating the great potential of TYUT-12 to achieve the challenging industrial separation of C_2H_4 from complex light hydrocarbon mixtures.

To gain insights into and comprehensively understand the interactions between the host and guest, we conducted density functional theory (DFT) simulations, aiming to pinpoint the specific adsorption sites within TYUT-12 and to quantify the said MOF's binding affinity toward C_3H_8, C_3H_6, C_2H_6, C_2H_4, C_2H_2, and CO_2 molecules. As shown in Fig. 5, the simulation results indicated that the alkane molecules (C_3H_8 and C_2H_6) were preferentially located in the annular interlayer channel (site I), where they engaged in multiple interactions with N and O atoms from TYUT-12 functional groups via strong C–H···O/N hydrogen bonds (2.51–3.01 Å). The preferential adsorption sites for the linear molecules (C_2H_2 and CO_2) were determined to be in site II, the narrow neck position in the annular interlayer channel, where several C–H···O/N hydrogen bonds (2.85–3.48 Å) were calculated to form between the TYUT-12 framework and the guest molecule. The preferential adsorption sites for the olefin molecules (C_3H_6 and C_2H_4) were calculated to be in site III, where the guest molecules engage in relatively weak C–H···π (2.85–3.46 Å) and π···π interactions (3.64–3.69 Å) with two benzene rings from the host. Importantly, given its larger molecular size than C_2H_4, C_3H_6 can interact more strongly than C_2H_4 with the host through extra C–H···O/N hydrogen bonds (2.87–3.19 Å). The data for the adsorption energy (E_{ads}) also shows that C_2H_4 has the minimum value among these gases (Table S7 in Appendix A). In a comparison of the DFT results for the series of TYUT-10/11/12/13 materials (Fig. S35 in Appendix A), the adsorption sites of C_2H_4 tended to be in the middle of the upper and lower layers and between the benzene rings, with TYUT-12 having the weakest interaction with C_2H_4. Significantly, the results from the theoretical calculations exhibited good consistency with the outcomes discussed in relation to the adsorption and breakthrough experiments.

To further verify the conformation of the C_2H_4 molecules adsorbed onto TYUT-12, high-resolution NPD experiments were conducted using a TYUT-12-D_7 sample synthesized using DMF-D_7 as the solvent. High-quality NPD data were collected at 10 K on C_2D_4-loaded TYUT-12 samples (Fig. 6 and Fig. S36 in Appendix A), allowing the conformation of the C_2H_4 molecules in the structure to be determined. As expected based on the results of the DFT calculations, the C_2H_4 molecules were found to be located in the flat round pores (site III), surrounded by six DMF molecules and sandwiched between two benzene rings (Figs. 6(e) and (f)). In this adsorption site, the C_2H_4 molecules engaged only in weak π···π interactions (3.47–3.76 Å) with the benzene rings—an outcome that shows good concurrence with the findings derived from the DFT calculations. Hence, through the collected NPD data, we confirmed the uniqueness of the adsorption environment of the C_2H_4 molecules in TYUT-12 and were able to explain the efficacy of the one-step C_2H_4 separation from binary, ternary, quaternary, and six-component C_2H_4-containing hydrocarbon mixtures.

In addition, the synthesis of TYUT-12 was scaled up, and the stability of this MOF was investigated, as shown in Fig. 7 and Figs. S37–S39 in Appendix A. Only easy-to-obtain chemical raw materials (i.e., nickel nitrate, H_3BTC, and DMF) are necessary for the preparation of TYUT-12, and the solvent after the reaction can be recycled; therefore, the synthesis of this MOF is relatively easy to scale up to the gram-level in the laboratory, and the samples prepared by this method maintain the original Brunauer–Emmett–Teller (BET) and adsorption properties. Notably, the powder X-ray diffraction (XRD) patterns of TYUT-12 were recorded after the material had undergone treatment under different

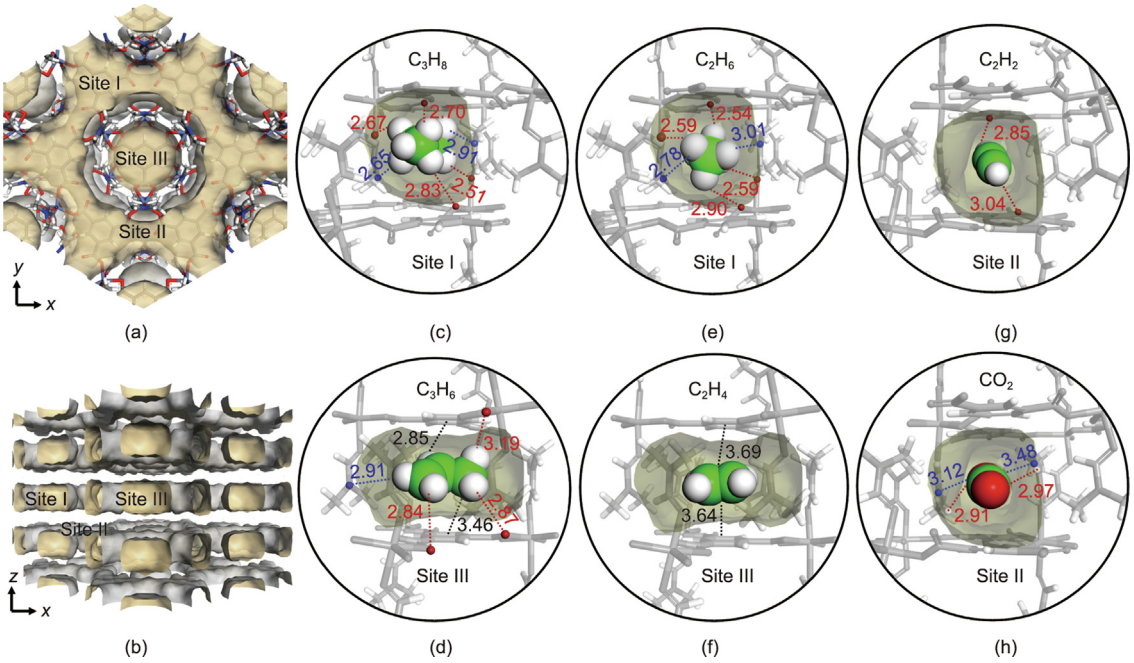

Fig. 5. (a, b) Preferential adsorption sites in TYUT-12 of (c) C_3H_8, (d) C_3H_6, (e) C_2H_6, (f) C_2H_4, (g) C_2H_2, and (h) CO_2, as obtained from DFT calculations (color code: Ni, cyan; C, gray; H, white; O, red; N, blue). Blue and red lines represent the interactions between the framework and gas molecules, respectively. Unit: Å.

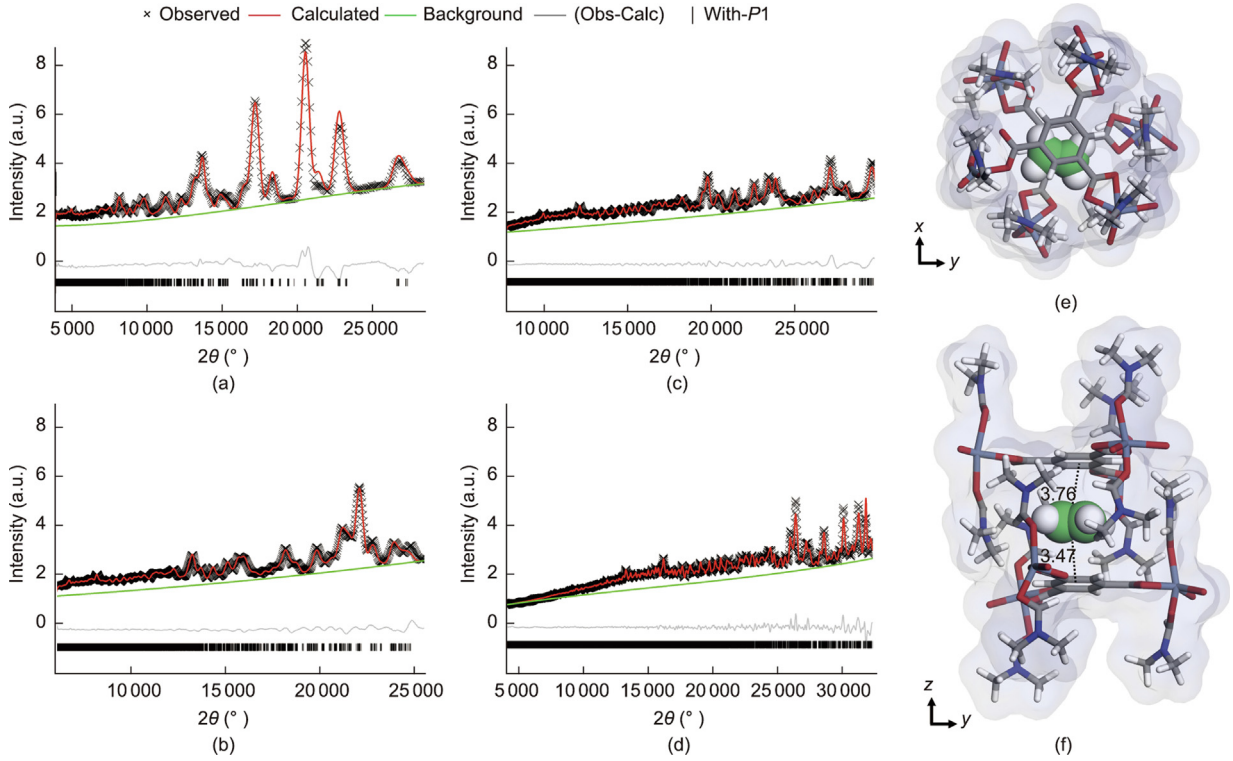

Fig. 6. NPD data. (a–d) Rietveld refinements of C_2D_4-loaded TYUT-12 collected from Banks 3–6 (NPD measured at 10 K). Goodness-of-fit parameters of the refinements: (a) R_{wp} = 0.0311; (b) R_{wp} = 0.0144; (c) R_{wp} = 0.0143; and (d) R_{wp} = 0.0163. (e, f) Corresponding adsorption site of C_2D_4 in TYUT-12.

conditions; these data indicated that TYUT-12 is characterized by a relatively stable structure. In detail, after being exposed to air for 18 months, no reduction in the C_2H_6 adsorption performance of TYUT-12 was observed. The crystal morphology after the stability test also remained (Fig. S38). Moreover, the stability of the material's dynamic adsorption of C_2H_6 was verified by conducting cyclic breakthrough experiments. TYUT-12 was able to maintain its C_2H_6 capture capacity over 20 breakthrough cycles, and its regeneration could be realized via a simple outgas process. Its dynamic C_2H_6 adsorption performance was also maintained for five cycles under humid conditions (75%) (Fig. S39). In summary, for the separation of C_2H_4 from multi-component light hydrocarbon mixtures,

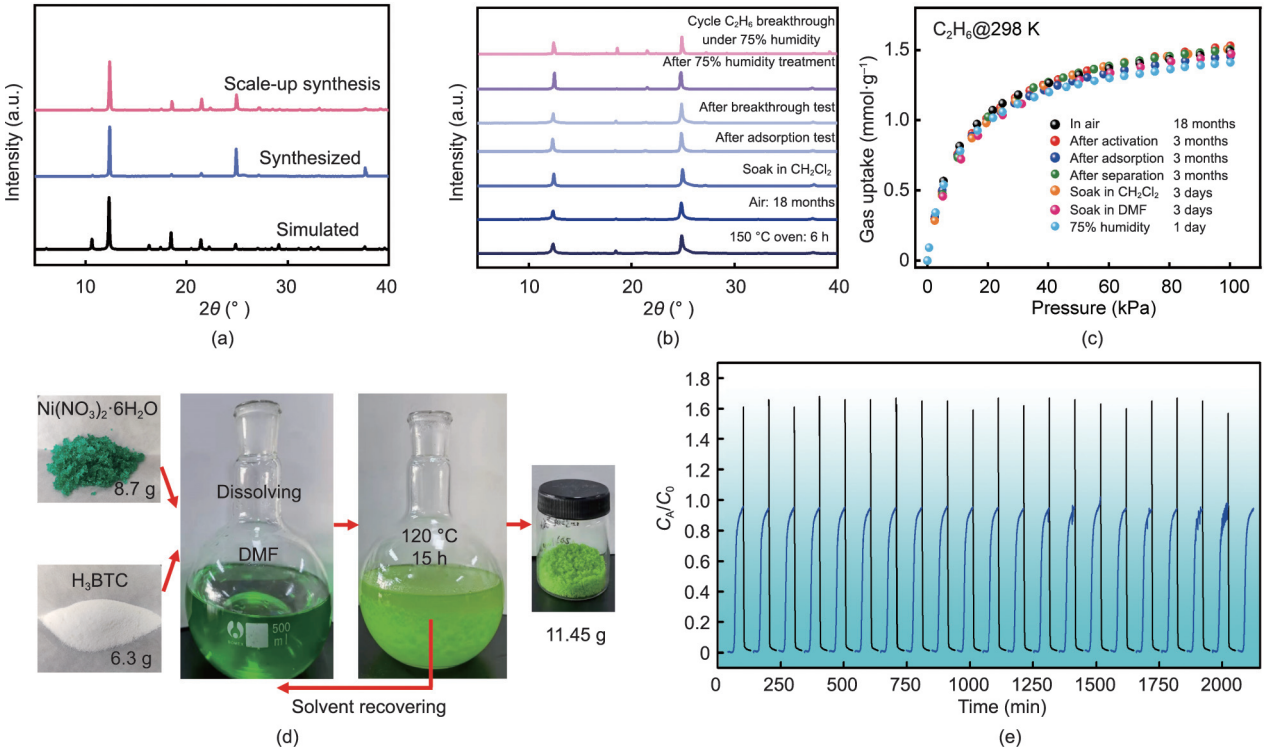

Fig. 7. Preparation and stability test results. (a, b) Simulated and experimental powder XRD patterns obtained for the as-synthesized MOF TYUT-12 and for the said material treated under different conditions. (c) C_2H_6 adsorption curves for TYUT-12 after the stability test. (d) Schematic representation of the gram-scale synthesis of TYUT-12 developed for up-scaling and solvent recycling. (e) Results of 20 cycles of C_2H_6 breakthrough (blue) and desorption (black) from TYUT-12.

TYUT-12 can be prepared via a simple, low-cost method, and the obtained material exhibits good structural and performance stability. These excellent characteristics demonstrate the great potential of this material for industrial applications.

4. Conclusions

This work demonstrates the successful construction of weak C_2H_4 adsorption locations through pore geometry design in a series of pillar-layered MOFs that can be used for the efficient one-step purification of C_2H_4. Based on its tailor-made pore environment, TYUT-12 exhibited outstanding adsorption selectivity for C_3H_8, C_3H_6, C_2H_6, C_2H_2, and CO_2 over C_2H_4; more specifically, its C_2H_6/C_2H_4 selectivity reached a value of 4.56, marking a new record for C_2H_4 purification from multi-component mixtures. Theoretical calculations and NPD analysis indicated that the targeted weak pore confinement of C_2H_4 in TYUT-12 was achieved via relatively weak π···π interactions (~3.6 Å) with two adjacent benzene rings. The results of the breakthrough experiments indicated that high-purity C_2H_4 (> 99.96%) was directly produced from $C_2H_6/C_2H_4/C_2H_2/CO_2$ quaternary mixtures and $C_3H_8/C_3H_6/C_2H_6/C_2H_4/C_2H_2/CO_2$ six-component mixtures through a one-step separation process. The pore segmentation strategy applied herein based on pore engineering and functional group regulation is an effective method to achieve the precise molecular recognition of target products; it also offers new solutions and routes to increase the efficiency and environmental friendliness of olefin separation strategies in the petrochemical industry.

Acknowledgments

The research work was supported by National Key Research and Development Program of China (2022YFB3806800) and National Natural Science Foundation of China (22278288 and 22090062). We gratefully acknowledge Juping Xu from the Spallation Neutron Source Science Center for the neutron powder diffraction.

Compliance with ethics guidelines

Yang Chen, Zhenduo Wu, Longlong Fan, Rajamani Krishna, Hongliang Huang, Yi Wang, Qizhao Xiong, Jinping Li, and Libo Li declare that they have no conflict of interest or financial conflicts to disclose.

Appendix A. Supplementary data

Supplementary data to this article can be found online at https://doi.org/10.1016/j.eng.2024.01.024.

References

[1] Bloch ED, Queen WL, Krishna R, Zadrozny JM, Brown CM, Long JR. Hydrocarbon separations in a metal–organic framework with open iron(II) coordination sites. Science 2012;335(6076):1606–10.
[2] Cui X, Chen K, Xing H, Yang Q, Krishna R, Bao Z, et al. Pore chemistry and size control in hybrid porous materials for acetylene capture from ethylene. Science 2016;353(6295):141–4.
[3] Dong Q, Huang Y, Hyeon-Deuk K, Chang IY, Wan J, Chen C, et al. Shape- and size-dependent kinetic ethylene sieving from a ternary mixture by a trap-and-flow channel crystal. Adv Funct Mater 2022;32(38):2203745.
[4] Liao PQ, Zhang WX, Zhang JP, Chen XM. Efficient purification of ethene by an ethane-trapping metal–organic framework. Nat Commun 2015;6:8697.
[5] Hao HG, Zhao YF, Chen DM, Yu JM, Tan K, Ma S, et al. Simultaneous trapping of C_2H_2 and C_2H_6 from a ternary mixture of $C_2H_2/C_2H_4/C_2H_6$ in a robust metal–organic framework for the purification of C_2H_4. Angew Chem Int Ed Engl 2018;57(49):16067–71.
[6] Zhang P, Zhong Y, Zhang Y, Zhu Z, Liu Y, Su Y, et al. Synergistic binding sites in a hybrid ultramicroporous material for one-step ethylene purification from ternary C_2 hydrocarbon mixtures. Sci Adv 2022;8(23):eabn9231.
[7] Gu XW, Wang JX, Wu E, Wu H, Zhou W, Qian G, et al. Immobilization of Lewis basic sites into a stable ethane-selective MOF enabling one-step separation of ethylene from a ternary mixture. J Am Chem Soc 2022;144(6):2614–23.

[8] Lin RB, Li L, Zhou HL, Wu H, He C, Li S, et al. Molecular sieving of ethylene from ethane using a rigid metal–organic framework. Nat Mater 2018;17(12):1128–33.
[9] Sholl DS, Lively RP. Seven chemical separations to change the world. Nature 2016;532(7600):435–7.
[10] Cadiau A, Adil K, Bhatt PM, Belmabkhout Y, Eddaoudi M. A metal–organic framework-based splitter for separating propylene from propane. Science 2016;353(6295):137–40.
[11] Yang Y, Li L, Lin RB, Ye Y, Yao Z, Yang L, et al. Ethylene/ethane separation in a stable hydrogen-bonded organic framework through a gating mechanism. Nat Chem 2021;13(10):933–9.
[12] Kong XJ, Li JR. An overview of metal–organic frameworks for green chemical engineering. Engineering. 2021;7(8):1115–39.
[13] Li J, Han X, Kang X, Chen Y, Xu S, Smith GL, et al. Purification of propylene and ethylene by a robust metal–organic framework mediated by host–guest interactions. Angew Chem Int Ed Engl 2021;60(28):15541–7.
[14] Li L, Lin RB, Krishna R, Li H, Xiang S, Wu H, et al. Ethane/ethylene separation in a metal–organic framework with iron–peroxo sites. Science 2018;362(6413):443–6.
[15] Chang M, Wang F, Wei Y, Yang Q, Wang JX, Liu D, et al. Separation of CH_4/N_2 by an ultra-stable metal–organic framework with the highest breakthrough selectivity. AIChE J 2022;68(9):e17794.
[16] Liang W, Xu F, Zhou X, Xiao J, Xia Q, Li Y, et al. Ethane selective adsorbent Ni(bdc)(ted)$_{0.5}$ with high uptake and its significance in adsorption separation of ethane and ethylene. Chem Eng Sci 2016;148:275–81.
[17] Chen Y, Du Y, Wang Y, Krishna R, Li L, Yang J, et al. A stable metal–organic framework with well-matched pore cavity for efficient acetylene separation. AIChE J 2021;67(5):e17152.
[18] Xian S, Peng J, Pandey H, Thonhauser T, Wang H, Li J. Robust metal–organic frameworks with high industrial applicability in efficient recovery of C_3H_8 and C_2H_6 from natural gas upgrading. Engineering 2023;23:56–63.
[19] Wang Y, Hao C, Fan W, Fu M, Wang X, Wang Z, et al. One-step ethylene purification from an acetylene/ethylene/ethane ternary mixture by cyclopentadiene cobalt-functionalized metal–organic frameworks. Angew Chem Int Ed Engl 2021;60(20):11350–8.
[20] Gu C, Hosono N, Zheng JJ, Sato Y, Kusaka S, Sakaki S, et al. Design and control of gas diffusion process in a nanoporous soft crystal. Science 2019;363(6425):387–91.
[21] Wang Y, Peh SB, Zhao D. Alternatives to cryogenic distillation: advanced porous materials in adsorptive light olefin/paraffin separations. Small 2019;15(25):1900058.
[22] Chen CX, Wei ZW, Pham T, Lan PC, Zhang L, Forrest KA, et al. Nanospace engineering of metal–organic frameworks through dynamic spacer installation of multifunctionalities for efficient separation of ethane from ethane/ethylene mixtures. Angew Chem Int Ed Engl 2021;60(17):9680–5.
[23] Ren Q. Advancements in MOF-based engineered materials for efficient separation processes. Engineering 2023;23:1–2.
[24] Li JR, Kuppler RJ, Zhou HC. Selective gas adsorption and separation in metal–organic frameworks. Chem Soc Rev 2009;38(5):1477–504.
[25] Furukawa H, Cordova KE, O'Keeffe M, Yaghi OM. The chemistry and applications of metal–organic frameworks. Science 2013;341(6149):1230444.
[26] Zeng H, Xie M, Wang T, Wei RJ, Xie XJ, Zhao Y, et al. Orthogonal-array dynamic molecular sieving of propylene/propane mixtures. Nature 2021;595(7868):542–8.
[27] Wang L, Huang H, Zhang X, Zhao H, Li F, Gu Y. Designed metal–organic frameworks with potential for multi-component hydrocarbon separation. Coord Chem Rev 2023;484:215111.
[28] Xu Z, Xiong X, Xiong J, Krishna R, Li L, Fan Y, et al. A robust Th-azole framework for highly efficient purification of C_2H_4 from a $C_2H_4/C_2H_2/C_2H_6$ mixture. Nat Commun 2020;11:3163.
[29] Zhu B, Cao JW, Mukherjee S, Pham T, Zhang T, Wang T, et al. Pore engineering for one-step ethylene purification from a three-component hydrocarbon mixture. J Am Chem Soc 2021;143(3):1485–92.
[30] Jiang Y, Hu Y, Luan B, Wang L, Krishna R, Ni H, et al. Benchmark single-step ethylene purification from ternary mixtures by a customized fluorinated anion-embedded MOF. Nat Commun 2023;14:401.
[31] Wu E, Gu XW, Liu D, Zhang X, Wu H, Zhou W, et al. Incorporation of multiple supramolecular binding sites into a robust MOF for benchmark one-step ethylene purification. Nat Commun 2023;14:6146.
[32] Chen KJ, Madden DG, Mukherjee S, Pham T, Forrest KA, Kumar A, et al. Synergistic sorbent separation for one-step ethylene purification from a four-component mixture. Science 2019;366(6462):241–6.
[33] Cao JW, Mukherjee S, Pham T, Wang Y, Wang T, Zhang T, et al. One-step ethylene production from a four-component gas mixture by a single physisorbent. Nat Commun 2021;12:6507.
[34] Laha S, Dwarkanath N, Sharma A, Rambabu D, Balasubramanian S, Maji TK. Tailoring a robust Al-MOF for trapping C_2H_6 and C_2H_2 towards efficient C_2H_4 purification from quaternary mixtures. Chem Sci 2022;13(24):7172–80.
[35] Sun H, Chen F, Chen R, Li J, Guo L, Liu Y, et al. Customizing metal–organic frameworks by lego-brick strategy for one-step purification of ethylene from a quaternary gas mixture. Small 2023;19(21):2208182.
[36] Lin RB, Wu H, Li L, Tang XL, Li Z, Gao J, et al. Boosting ethane/ethylene separation within isoreticular ultramicroporous metal–organic frameworks. J Am Chem Soc 2018;140(40):12940–6.
[37] Li B, Wen HM, Cui Y, Zhou W, Qian G, Chen B. Emerging multifunctional metal–organic framework materials. Adv Mater 2016;28(40):8819–60.
[38] Fan W, Yuan S, Wang W, Feng L, Liu X, Zhang X, et al. Optimizing multivariate metal–organic frameworks for efficient C_2H_2/CO_2 separation. J Am Chem Soc 2020;142(19):8728–37.
[39] Jeong S, Kim D, Shin S, Moon D, Cho SJ, Lah MS. Combinational synthetic approaches for isoreticular and polymorphic metal–organic frameworks with tuned pore geometries and surface properties. Chem Mater 2014;26(4):1711–9.
[40] Gao C, Liu S, Xie L, Ren Y, Cao J, Sun C. Design and construction of a microporous metal–organic framework based on the pillared-layer motif. CrystEngComm 2007;9(7):545–7.
[41] Bruker. SAINT. Madison: Bruker AXS, Inc.; 2009.
[42] Sheldrick GM. SADABS: program for empirical absorption correction. Gottingen: University of Gottingen; 1996.
[43] Sheldrick GM. A short history of SHELX. Acta Crystallogr Sect A Found Adv 2008;64(Pt 1):112–22.
[44] Xu J, Xia Y, Li Z, Chen H, Wang X, Sun Z, et al. Multi-physics instrument: total scattering neutron time-of-flight diffractometer at China Spallation Neutron Source. Nucl Instrum Methods Phys Res Sect A 2021;1013:165642.
[45] Xiao Y, Liu T, Liu J, He L, Chen J, Zhang J, et al. Insight into the origin of lithium/nickel ions exchange in layered $Li(Ni_xMn_yCo_z)O_2$ cathode materials. Nano Energy 2018;49:77–85.
[46] Lv D, Zhou P, Xu J, Tu S, Xu F, Yan J, et al. Recent advances in adsorptive separation of ethane and ethylene by C_2H_6-selective MOFs and other adsorbents. Chem Eng J 2022;431(Pt 3):133208.
[47] Krishna R. Synergistic and antisynergistic intracrystalline diffusional influences on mixture separations in fixed-bed adsorbers. Precis Chem 2023;1(2):83–93.

Supplementary data for

Direct Ethylene Purification from Cracking Gas via a Metal–Organic Framework Through Pore Geometry Fitting

Yang Chen [a,#], Zhenduo Wu [b,f,#], Longlong Fan [c,#], Rajamani Krishna [d], Hongliang Huang [e], Yi Wang [a], Qizhao Xiong [a], Jinping Li [a,*], Libo Li [a,*]

[a] *College of Chemical Engineering and Technology, Taiyuan University of Technology, Taiyuan 030024, China*
[b] *City University of Hong Kong (Dongguan), Dongguan 523000, China*
[c] *Institute of High Energy Physics, Chinese Academy of Sciences, Beijing 100049, China*
[d] *Van't Hoff Institute for Molecular Sciences, University of Amsterdam, Amsterdam 1098 XH, Netherlands*
[e] *State Key Laboratory of Separation Membranes and Membrane Processes, Tiangong University, Tianjin 300387, China*
[f] *Center for Neutron Scattering, City University of Hong Kong Shenzhen Research Institute, Shenzhen 518057, China*

* Corresponding authors.
E-mails addresses: jpli211@hotmail.com (J. Li), lilibo@tyut.edu.cn (L. Li).
[#] These authors contributed equally to this work.

S1. Chemicals

All starting chemicals and solvents were commercially available and directly used without further purification: nickel nitrate hexahydrate ($Ni(NO_3)_2 \cdot 6H_2O$, 99.0%), trimesic acid (H_3BTC, 98.0%), 4,4′-bipyridine (98.0%), pyrazine (99.0%), pyridine (99.5%), and *N*,*N*-dimethylformamide-D_7 (DMF-D_7, D 99.5%) were purchased from Aladdin Reagent Co., Ltd. (China); *N*,*N*-dimethylformamide (DMF, 99.7%) was obtained from Sinopharm Group Chemical Reagent Co., Ltd. (China); Deionized water was purified by using a Millipore Elix Advantage 3 purification system.

Pure gas C_3H_8 (99.99%), C_3H_6 (99.99%), C_2H_6 (99.99%), C_2H_4 (99.99%), C_2H_2 (99.99%), CO_2 (99.999%), He (99.999%), and binary mixed gases of C_3H_8/C_2H_4 (v/v 50:50), C_3H_6/C_2H_4 (v/v 50:50), C_2H_6/C_2H_4 (v/v 50:50 and 10:90), C_2H_2/C_2H_4 (v/v 50:50), and CO_2/C_2H_4 (v/v 50:50), multi-component mixtures of $C_2H_6/C_2H_4/C_2H_2$ (v/v/v 9:90:1), $C_2H_6/C_2H_4/C_2H_2/CO_2$ (v/v/v/v 9:89:1:1 and 9:85:1:5) and $C_3H_8/C_3H_6/C_2H_6/C_2H_4/C_2H_2/CO_2$ (v/v/v/v/v/v 9:9:10:70:1:1) were purchased from Beijing Special Gas Co., Ltd. (China).

S2. Characterization

The crystallinity and phase purity of the materials were checked by powder X-ray diffraction (PXRD) on a Bruker D8 ADVANCE X-ray diffractometer with Cu Kα (λ = 1.54184 Å) radiation operated at 40 kV and 40 mA. Scanning was performed over the 2θ range of 5–40 °at 4(°)·min^{-1}. The TGA of the samples was collected on a thermal analyzer (NETZSCH, STA 449 F5) at a heating rate of 10 ℃·min^{-1} under air atmosphere. N_2 and CO_2 adsorption/desorption isotherms were obtained using an ASAP 2020 Plus HD88 analyzer at 77 and 196 K, respectively.

S3. Stability test

The samples are exposed to the air and the ambient humidity is between 25% and 60%. During the water stability test, flowing air with a humidity of 75% was used for purging for 1 day. In the C_2H_6 breakthrough experiment for TYUT-12 under humid conditions (75%), dry C_2H_6 is wetted and then dynamically adsorbed under humid conditions. After the adsorption test, separation test, solvent immersion, and water stability test, the samples were characterized by PXRD and SEM.

S4. Density functional theory (DFT) calculations

The periodic structure of TYUT-12 used on the DFT calculations in this work is constructed from the reported crystallography structure [1]. And the periodic TYUT-12 unit cell had 258 atoms with a lattice constant of 16.609 Å × 16.609 Å × 14.325 Å, $\alpha = \beta = 90.0$ °, $\gamma = 120.0$ °. The adsorption energy (E_{ads}) of an adsorbate, that is, C_3H_8, C_3H_6, C_2H_6, C_2H_4, C_2H_2, and CO_2 molecule in the pore cavities of TYUT-12 were calculated using the following equation:

$$E_{\text{ads}} = E_{\text{adsobate/MOF}} - (E_{\text{MOF}} + E_{\text{adsorbate}}) \quad \text{(S1)}$$

where $E_{\text{adsobaste/MOF}}$, E_{MOF}, and $E_{\text{adsobaste}}$ represent the total energies of the adsorbate interacting with TYUT-12, the pristine TYUT-12, and the adsorbate molecule in vacuum. A negative E_{ads} value indicates the favorable adsorption of the adsorbate.

First-principles-based computational details

All DFT calculations were carried out using the Quickstep program within the framework of the CP2K code with mixed Gaussian and plane-wave basis sets [2,3]. The generalized gradient approximation for exchange-correlation functional of Perdew–Burke–Enzerhof (PBE) was adopted in the calculations [4]. The energy cutoff was set as of 360 Ry (1 Ry = 2.1798741 × 10^{-18} J. The core electron was represented by norm-conserving Goedecker–Teter–Hutter pseudopotentials [5–

7]. The valance electron wave function was expanded in a double-zeta basis set with polarization functions along with an auxiliary plane wave basis set. Each configuration was optimized with the Broyden–Fletcher–Goldfarb–Shanno (BFGS) algorithm with the self-consistent field (SCF) convergence criteria of 1.0×10^{-8} a.u. The DFT-D3 scheme with an empirical damped potential term was added into the energies to compensate the long-range van der Waads (vdW) dispersion interaction between the adsorbates and the TYUT-12 skeleton [8].

Using the above method, preferential adsorption sites of C_2H_4 in TYUT-10, TYUT-11, and TYUT-13 were also obtained.

S5. Fitting of unary isotherms

The unary isotherm data for C_3H_8, C_3H_6, C_2H_6, C_2H_4, C_2H_2, and CO_2 measured at two different temperatures 273 K, and 298 K in TYUT-12 were fitted with good accuracy using 1-site Langmuir–Freundlich model:

$$q = \frac{q_{sat} b p^{v}}{1 + b p^{v}} \qquad \text{(S2)}$$

In Eq. (S2), the Langmuir–Freundlich parameter b is temperature dependent

$$b = b_0 \exp\left(\frac{E}{RT}\right) \qquad \text{(S3)}$$

In Eq. (S3), E is the energy parameter. The fit parameters are provided in Table S1.

S6. Ideal adsorption solution theory (IAST) calculation

For screening MOFs for separation of binary mixtures of components 1 and 2, the adsorption selectivity, S_{ads}, is defined by

$$S_{ads} = \frac{q_1 / q_2}{y_{10} / y_{20}} \qquad \text{(S4)}$$

In Eq. (S4), y_{10} and y_{20} are the mole fractions of the bulk gas phase mixture.

The molar loadings q_1 and q_2 of the two components are determined using the IAST of Myers and Prausnitz using the unary isotherm fits as data inputs [9].

S7. Calculations of isosteric heat of adsorption (Q_{st})

Using the data collected of adsorption isotherms at 273–298 K to calculate the isosteric enthalpy. The data was fitted using a virial-type expression composed of parameters a_i and b_i. Then, the Q_{st} (kJ·mol^{-1}) was calculated from the fitting parameters using (Eq. (S5)), where p is the pressure (bar), T is the temperature (K), R is the universal gas constant (8.314 J·mol^{-1}·K^{-1}), N is the amount adsorbed (mmol·g^{-1}), and m and n determine the number of terms required to adequately describe the isotherm.

The virial equation be written as follows:

$$\ln p = \ln N + \frac{1}{T}\sum_{i=0}^{m} a_i N_i + \sum_{i=0}^{n} b_i N_i \qquad \text{(S5)}$$

The calculation formula for isosteric enthalpies of adsorption:

$$Q_{st} = -R\sum_{i=0}^{m} a_i N_i \qquad \text{(S6)}$$

S8. Transient unary uptakes

The radial distribution of molar loadings, q_i, within a spherical MOF crystallite, of radius R_c, is obtained from a solution of a set of differential equations describing the uptake:

$$\rho \frac{\partial q_i(r,t)}{\partial t} = -\frac{1}{r^2}\frac{\partial}{\partial r}\left(r^2 N_i\right) \qquad \text{(S7)}$$

The intra-crystalline fluxes N_i in Eq. (S7) are related to chemical potential gradients by the Maxwell–Stefan (M–S) diffusion formulation [10–12]

$$N_i = -\rho Đ_i \frac{q_i}{RT}\frac{\partial \mu_i}{\partial r} \qquad \text{(S8)}$$

In Eqs. (S7) and (S8), R is the gas constant, T is the temperature, ρ represents the framework density of the microporous crystalline material, r is the radial distance coordinate, and the component loadings q_i are defined in terms of moles per kilogram of framework. The $Đ_i$ characterize and quantify the interaction between species i and pore walls. At any time, t, during the transient approach to thermodynamic equilibrium, the spatial-averaged component loading within the crystallites of radius R_c is calculated using

$$\bar{q}_i(t) = \frac{3}{r_c^3}\int_0^{r_c} q_i(r,t) r^2 \mathrm{d}r \qquad \text{(S9)}$$

The spatial-averaged loadings $\bar{q}_i(t)$ can be compared directly with experimental transient uptake data for unary guests. The numerical details for solution of the set of partial differential equations is provided in earlier works [13]. The values of the diffusional time constants, fitted to the experimental data are provided in Table S2.

S9. Calculation for C_2H_4 capture amount and productivity at dynamic condition

The calculation for the adsorption amount of C_2H_4 during the breakthrough process in TYUT-12 is defined by [14]

$$Q_{\max} = q\int_0^{\infty}\left[c_i^0 - c_i(t)\right]\mathrm{d}t \qquad \text{(S10)}$$

The calculation for the C_2H_4 productivity in the different breakthrough experiments is defined by

$$P = qt_{\mathrm{n}} - q\int_0^{\infty}\left[c_i^0 - c_i(t)\right]\mathrm{d}t \qquad \text{(S11)}$$

In the adsorption process before the quaternary mixtures breakthrough point (0–t_1), the captured C_2H_4 of TYUT-12 is calculated to be 0.74 mmol·g^{-1}. Considering the continuous C_2H_4 adsorption during the mass transfer zone (t_1–t_2), the integration of the entire breakthrough curve gave the maximum loading of TYUT-12 to be 0.90 mmol·g^{-1} (grey area). By using the same method, we can calculate the adsorbed amount of C_2H_4 in the binary, ternary, and six-component mixtures breakthrough experiment were 0.83, 0.95, and 0.86 mmol·g^{-1}, respectively. For the calculation of C_2H_4 productivity in the different breakthrough experiments (blue area in Fig. S23), the value was 0.36, 0.80, 0.78, and 0.60 mmol·g^{-1}, respectively. $Q_{\max}$ is the maximum capture of C_2H_4; P is the productivity of C_2H_4, q is the flow rate of C_2H_4, t_{n} is the earliest breakthrough time of other gases except C_2H_4.

Notation

b	Langmuir–Freundlich parameter, Pa^{-v}
$Đ_i$	Maxwell–Stefan diffusivity for molecule-wall interaction, m^2·s^{-1}
E	energy parameter, J·mol^{-1}
L	length of packed bed adsorber, m
m^{ads}	mass of adsorbent in packed bed, kg
n	number of species in the mixture
N_i	molar flux of species i with respect to framework, mol·m^{-2}·s^{-1}
p_i	partial pressure of species i in mixture, Pa
p_{t}	total system pressure, Pa
q_i	component molar loading of species i, mol·kg^{-1}
$q_{i,\mathrm{sat}}$	molar loading of species i at saturation, mol·kg^{-1}
q_{t}	total molar loading in mixture, mol·kg^{-1}
$\bar{q}_i(t)$	spatial-averaged component uptake of species i, mol·kg^{-1}
Q_0	volumetric flow rate of gas mixture at inlet to fixed bed, m^3·s^{-1}
r	radial direction coordinate, m
R_{c}	radius of crystallite, m
R	gas constant, 8.314 J·mol^{-1}·K^{-1}
t	time, s
S_{ads}	adsorption selectivity
t	time, s
T	absolute temperature, K
u	superficial gas velocity in packed bed, m·s^{-1}
v	interstitial gas velocity in packed bed, m·s^{-1}
x_i	mole fraction of species i in adsorbed phase
y_i	mole fraction of species i in the bulk fluid phase

Greek alphabet

μ_i	molar chemical potential of species i, J·mol^{-1}
v	Freundlich exponent
ρ	framework density, kg·m^{-3}

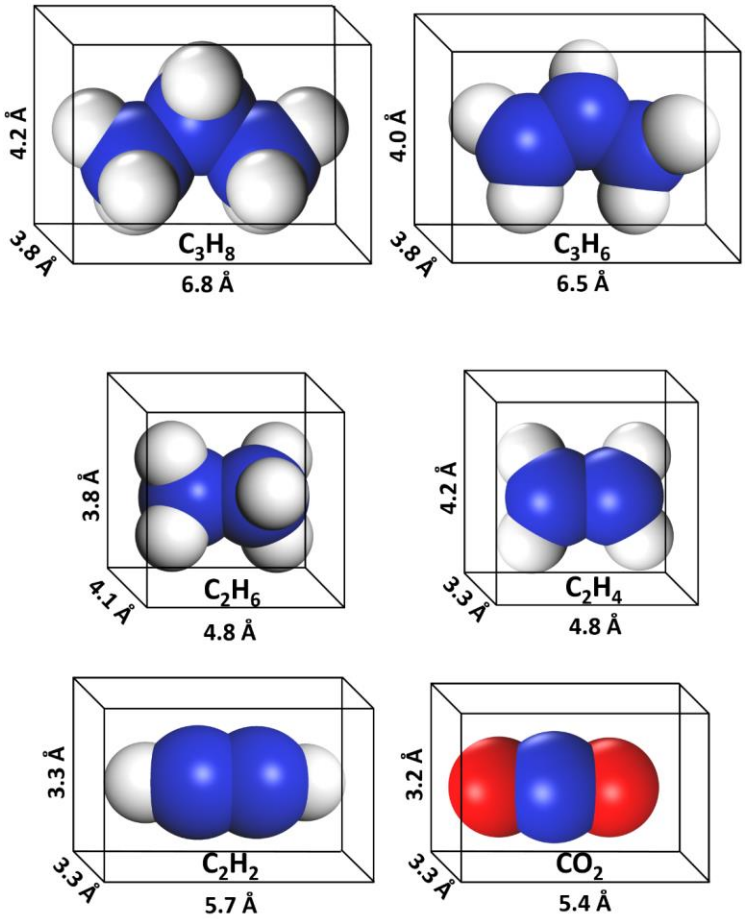

Fig. S1. Comparison of molecular geometry of C_3H_8, C_3H_6, C_2H_6, C_2H_4, C_2H_2, and CO_2 (color code: O, red; C, blue; H, white).

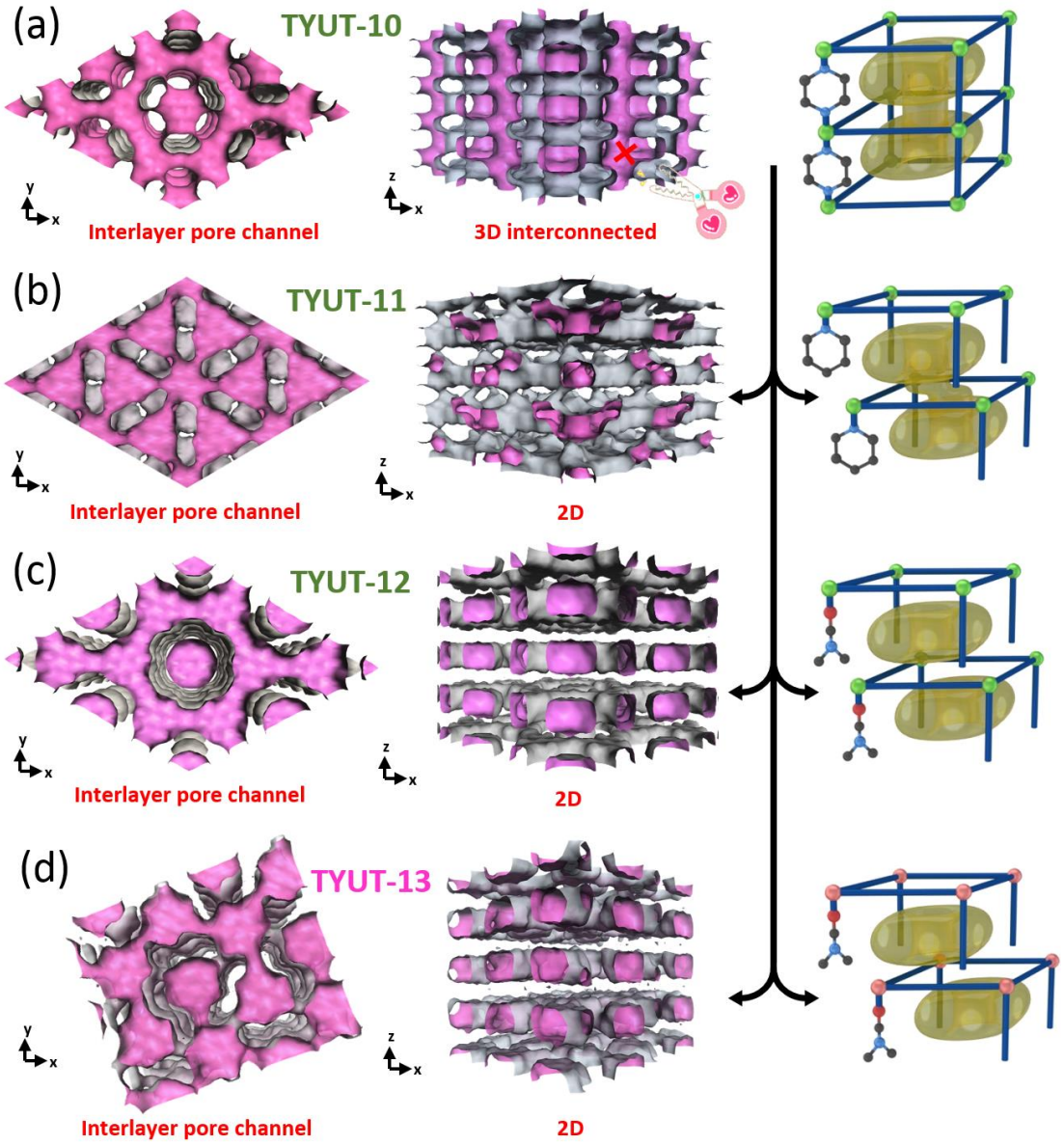

Fig. S2. Schematic diagram of the structural change of the interlayer channel from TYUT-10 to TYUT-14.

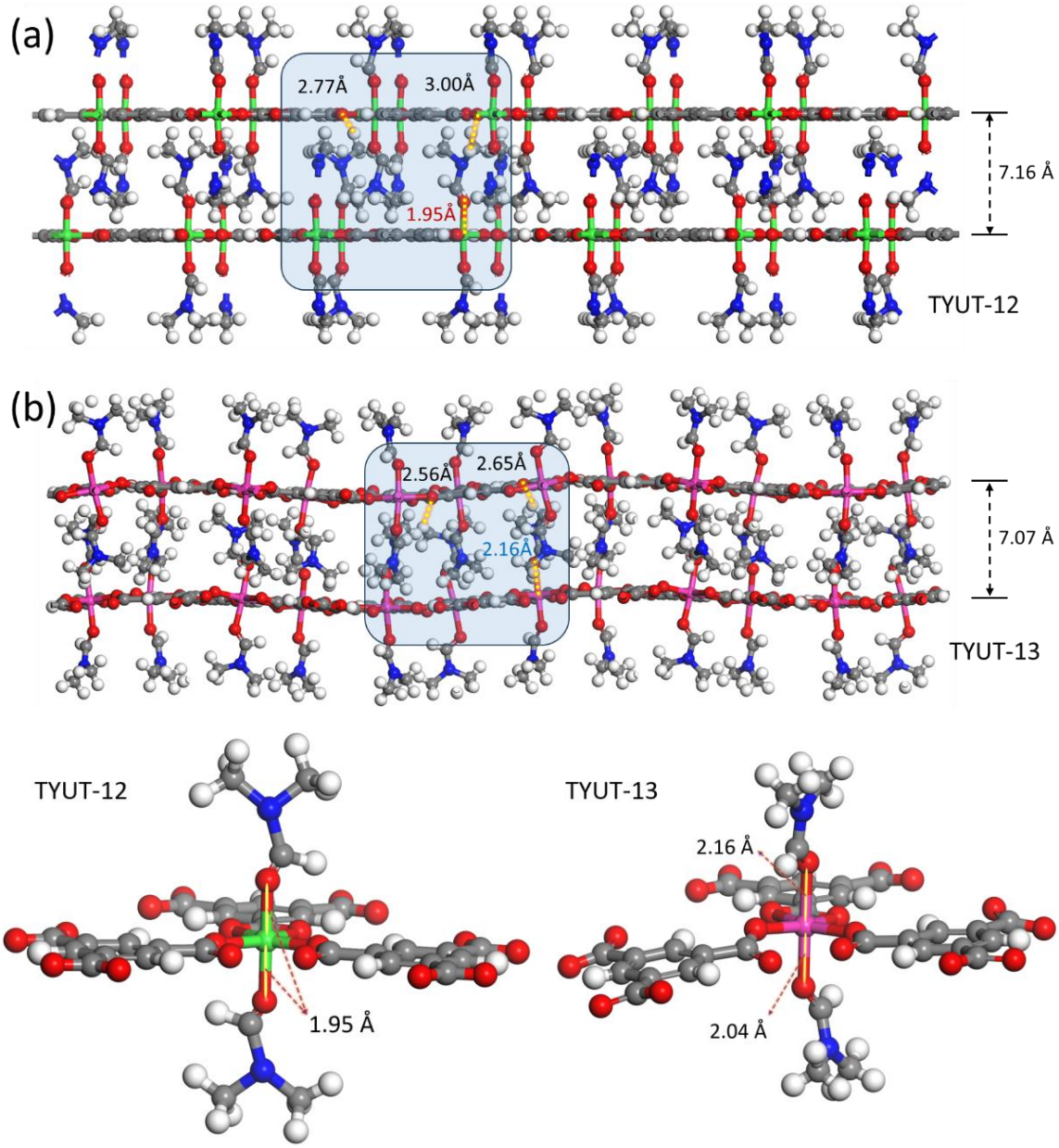

Fig. S3. Comparison of structural differences between (a) TYUT-12 and (b) TYUT-13.

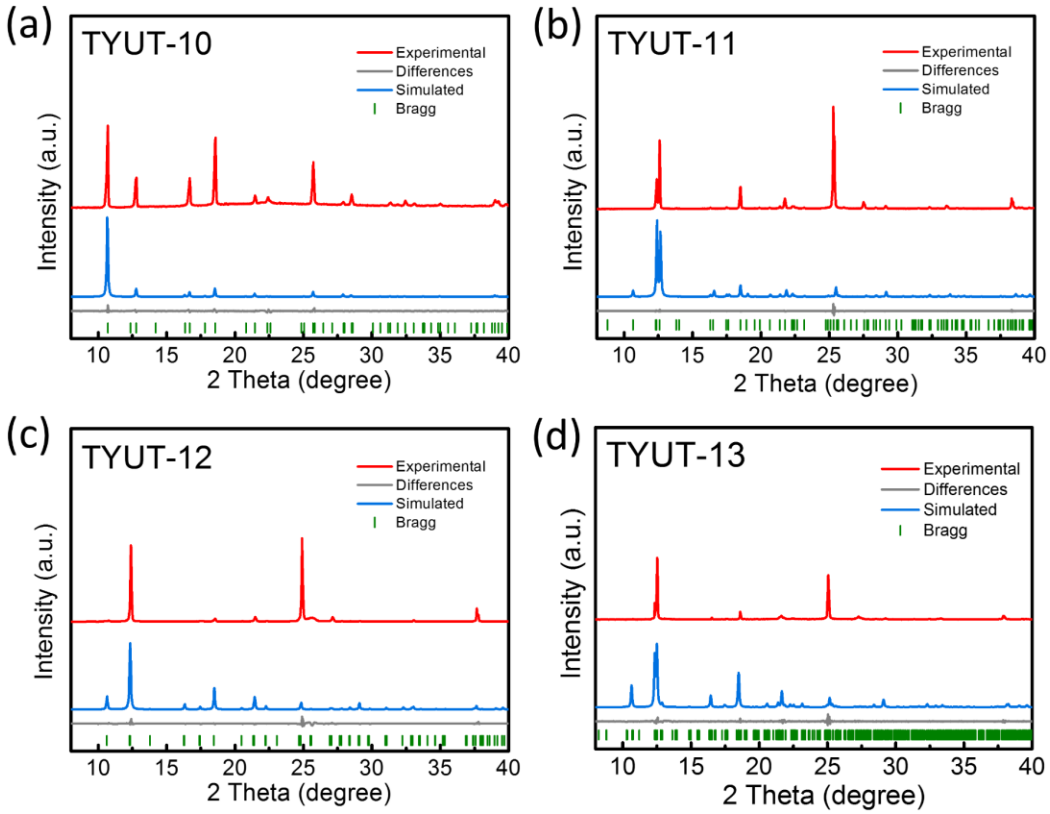

Fig. S4. Rietveld-refined PXRD patterns of TYUT-10 (R_p = 6.68%, R_{wp} = 8.96%), TYUT-11 (R_p = 9.06%, R_{wp} = 12.1%), TYUT-12 (R_p = 9.4%, R_{wp} = 12.7%), and TYUT-13 (R_p = 8.46%, R_{wp} = 11.6%).

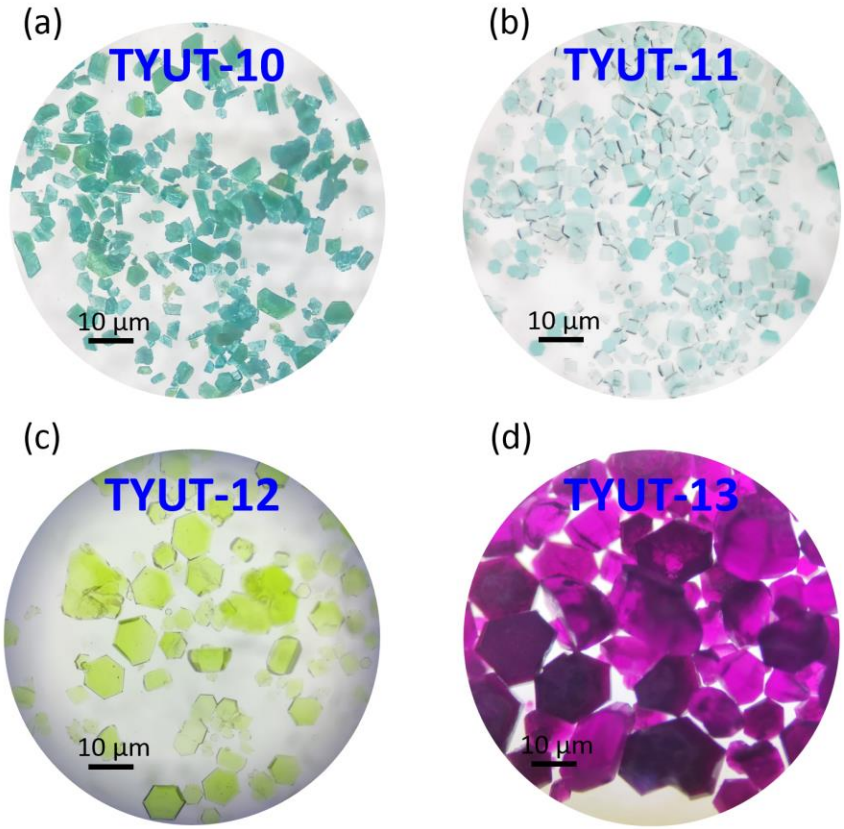

Fig. S5. Optical microscope photos of TYUT-10, TYUT-11, TYUT-12, and TYUT-13.

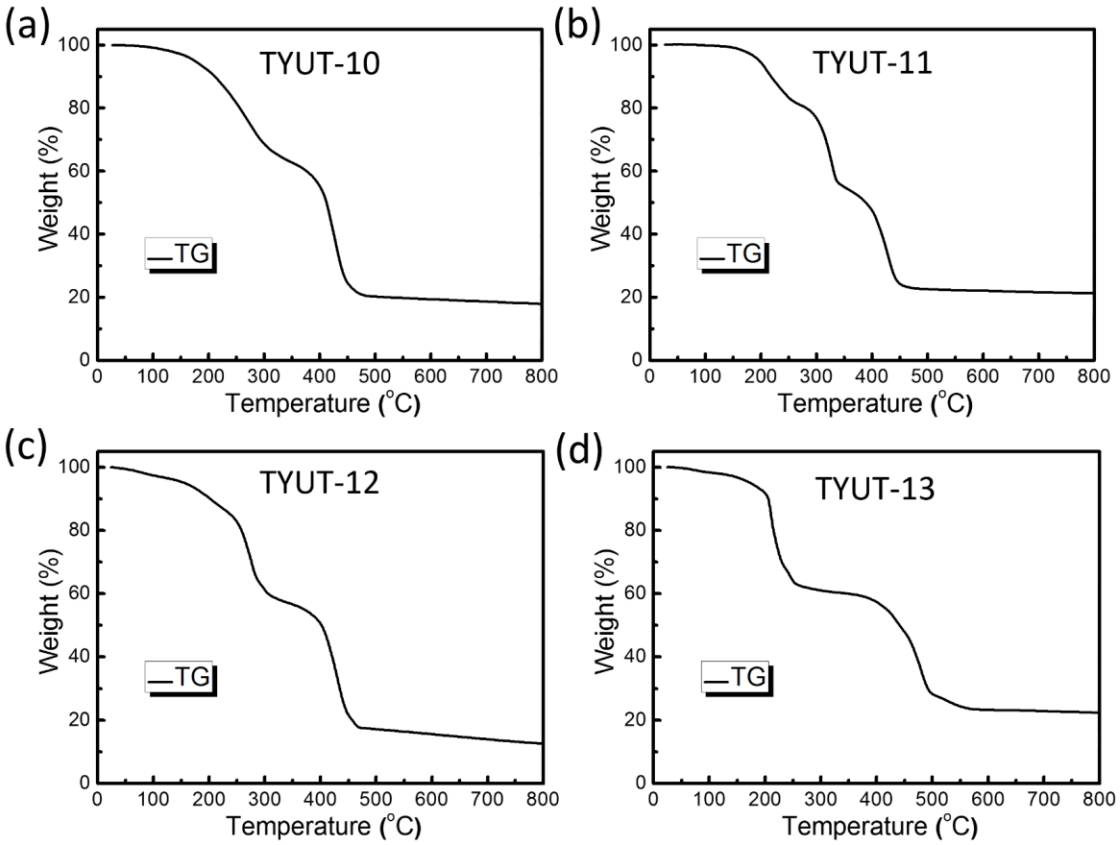

Fig. S6. Thermogravimetric curves of TYUT-10, TYUT-11, TYUT-12, and TYUT-13.

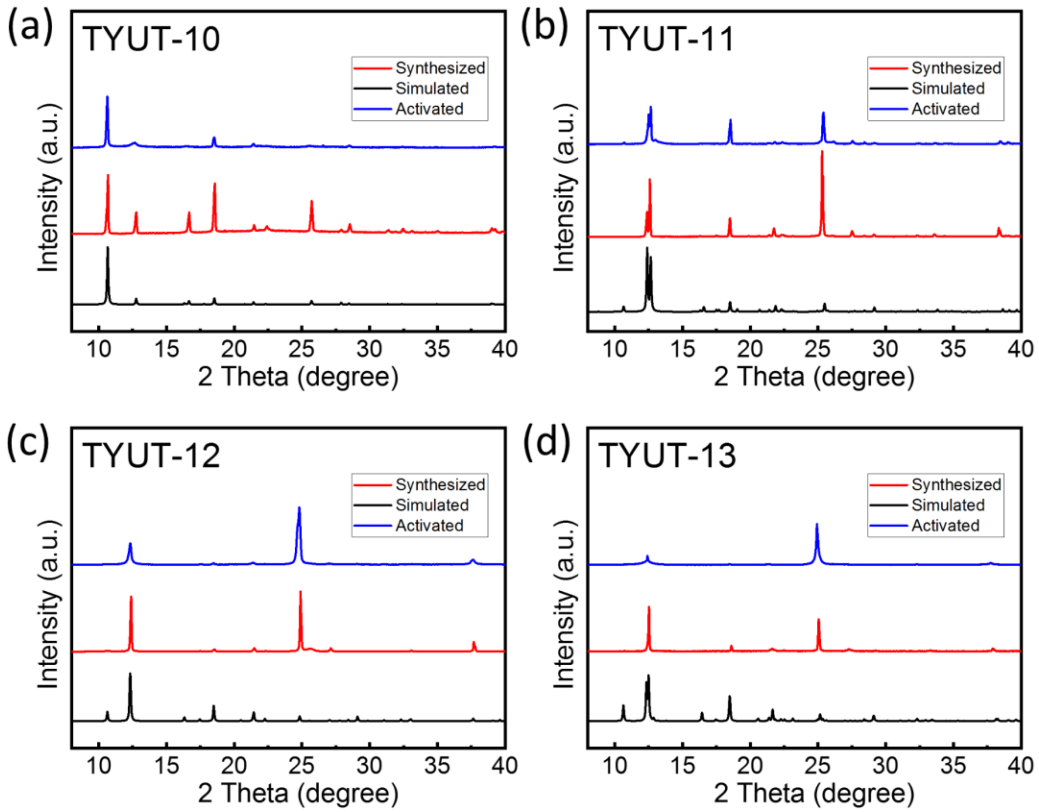

Fig. S7. Synthesized and activated powder X-ray diffractometry patterns for TYUT-10, TYUT-11, TYUT-12, and TYUT-13.

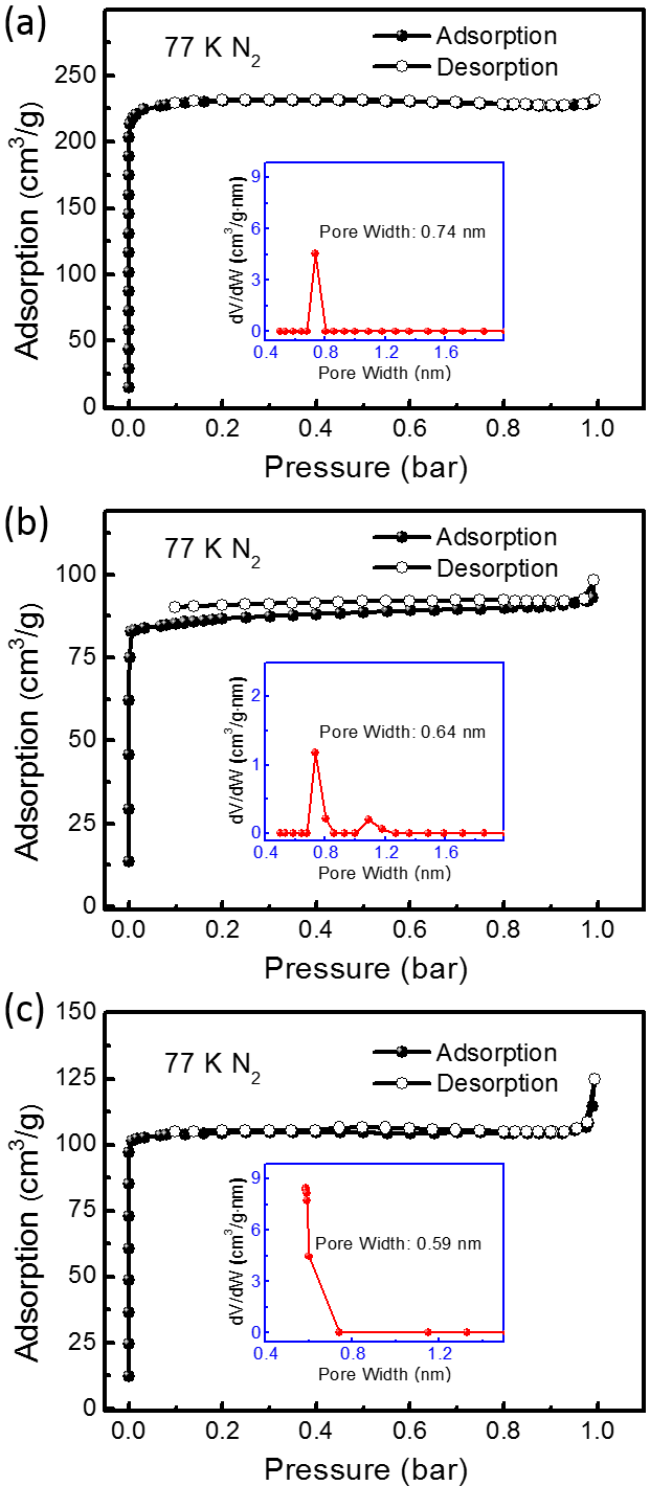

Fig. S8. N_2 adsorption/desorption isotherms at 77 K and the corresponding pore size distribution of (a) TYUT-10, (b) TYUT-11, and (c) TYUT-12.

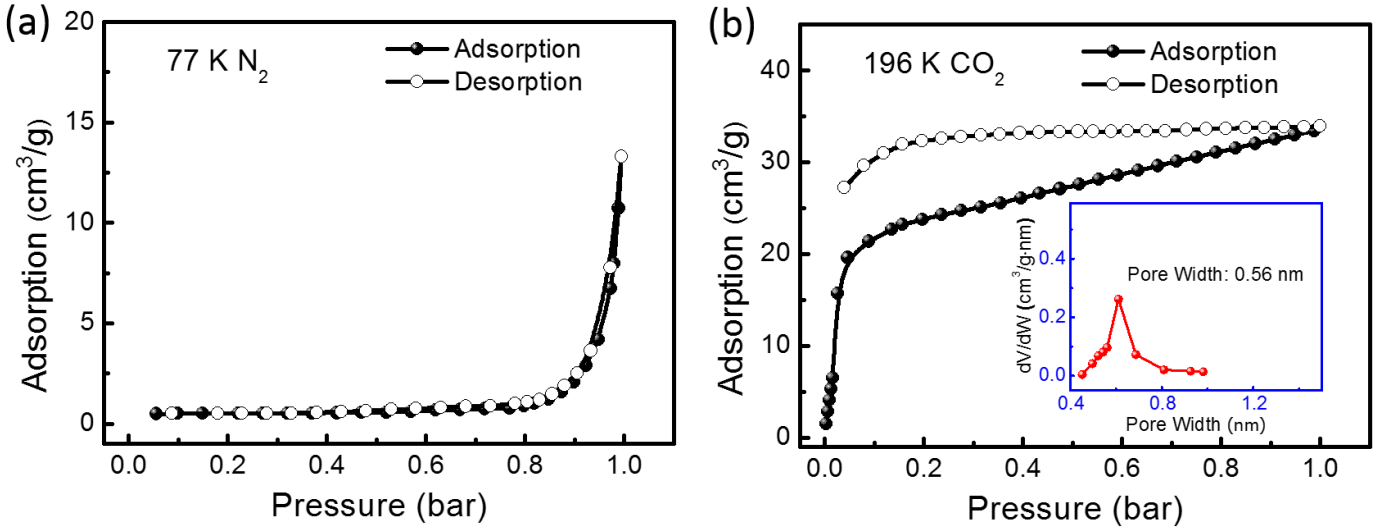

Fig. S9. N_2 (77 K) and CO_2 (196 K) adsorption/desorption isotherms and the corresponding pore size distribution of TYUT-13.

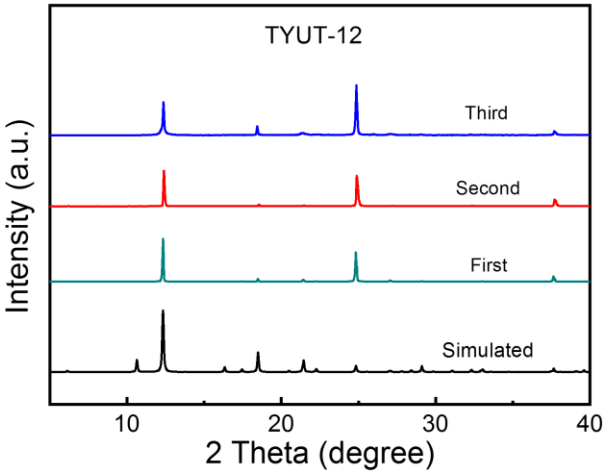

Fig S10. PXRD patterns of TYUT-12 sample prepared using recycled DMF-D7.

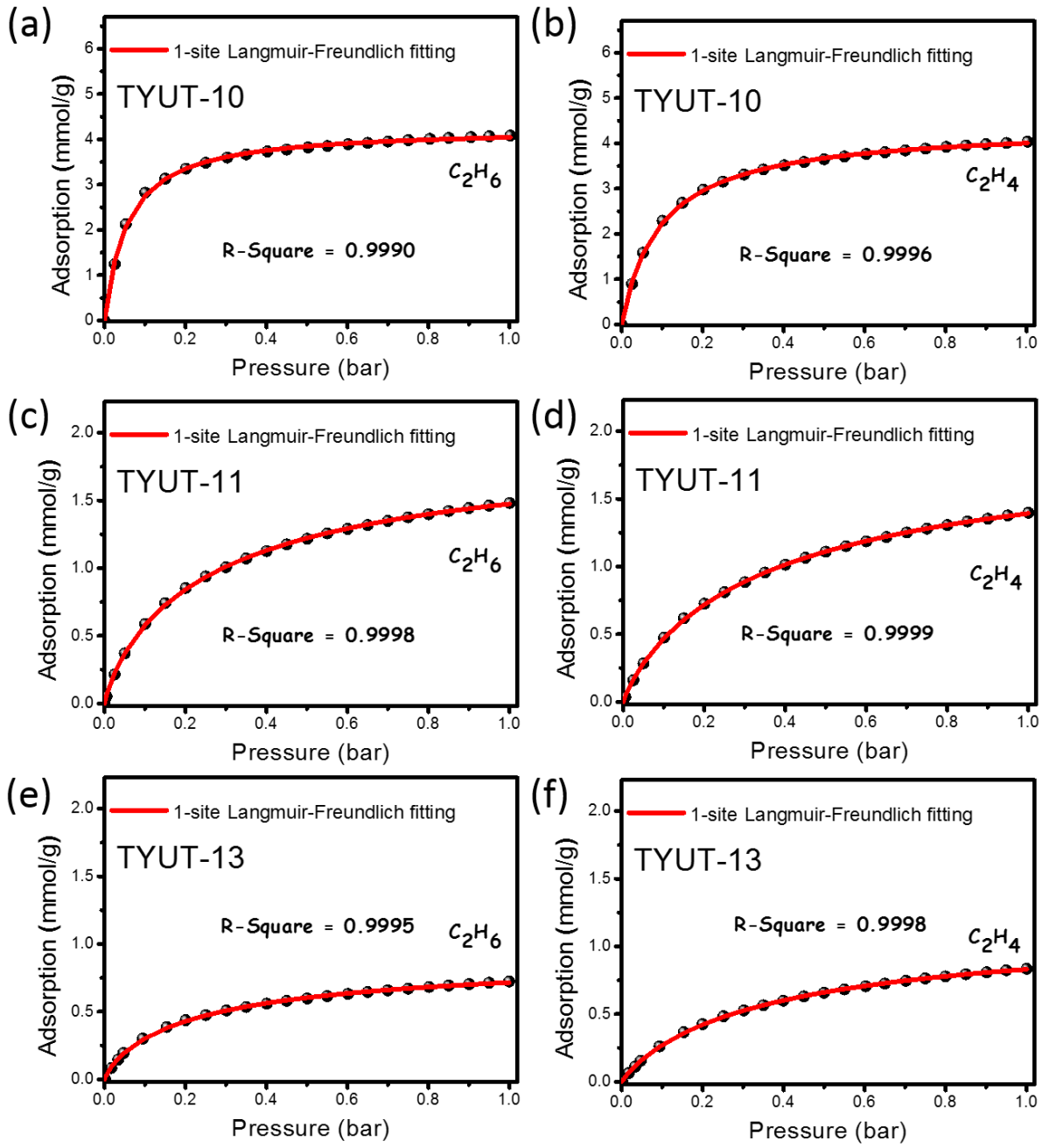

Fig. S11. C_2H_6 and C_2H_4 adsorption isotherms at 298 K for TYUT-10, TYUT-11, and TYUT-13 with 1-site Langmuir–Freundlich model fits.

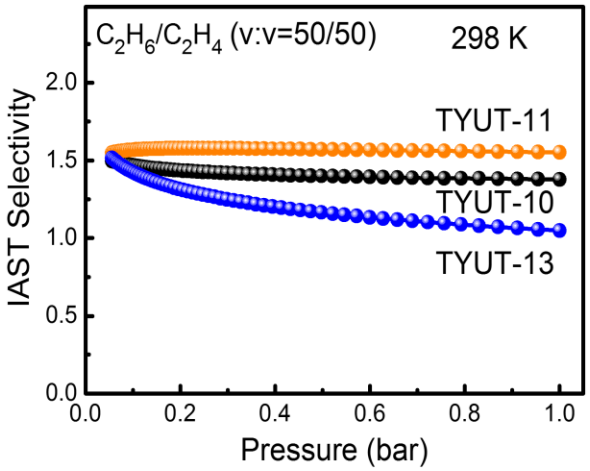

Fig. S12. IAST selectivities of C_2H_6/C_2H_4 mixtures (v/v 50:50) at 298 K for TYUT-10, TYUT-11, and TYUT-13.

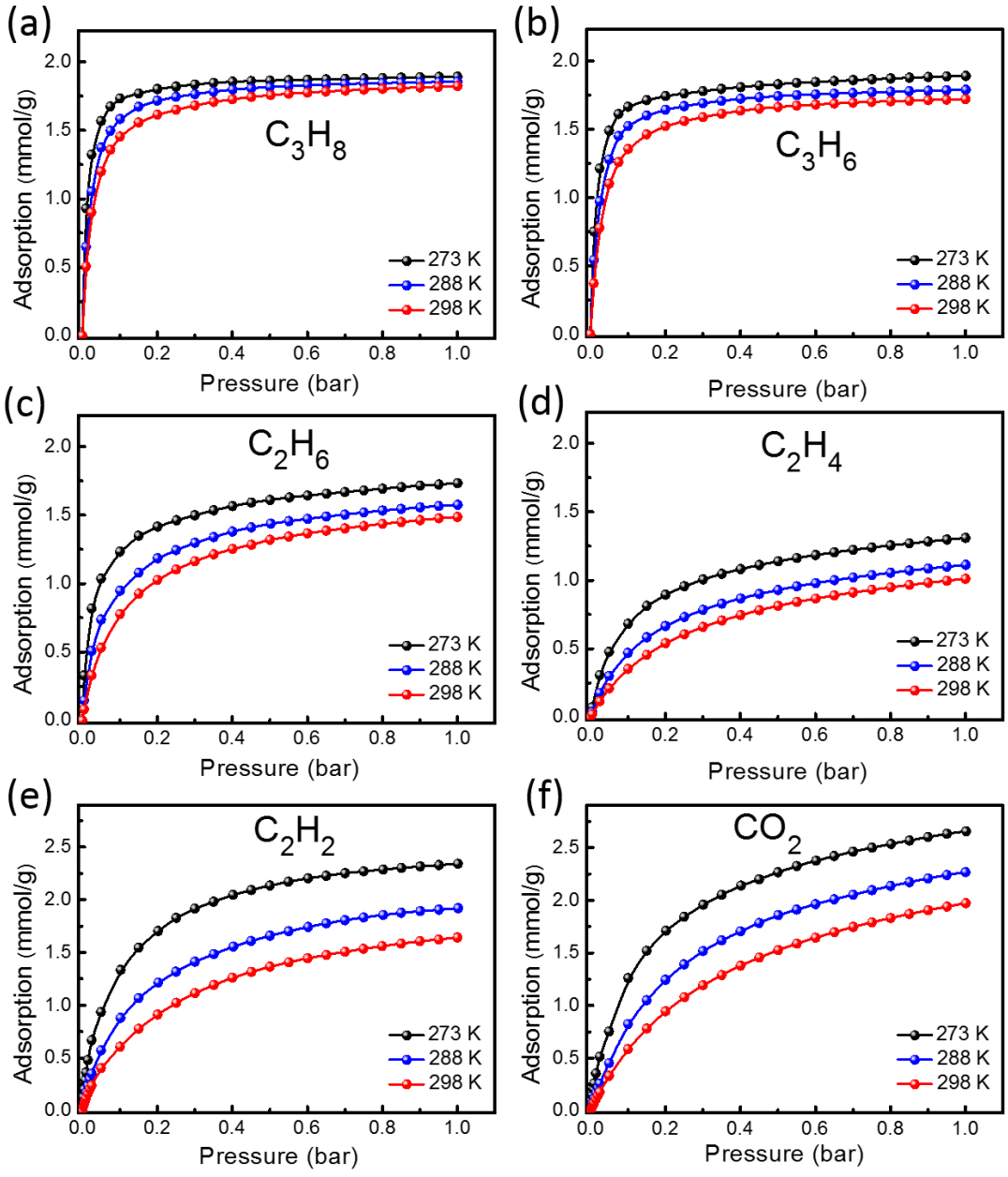

Fig. S13. Single-component gas adsorption isotherms of C_3H_8, C_3H_6, C_2H_6, C_2H_4, C_2H_2, and CO_2 on TYUT-12 at 273, 288, and 298 K.

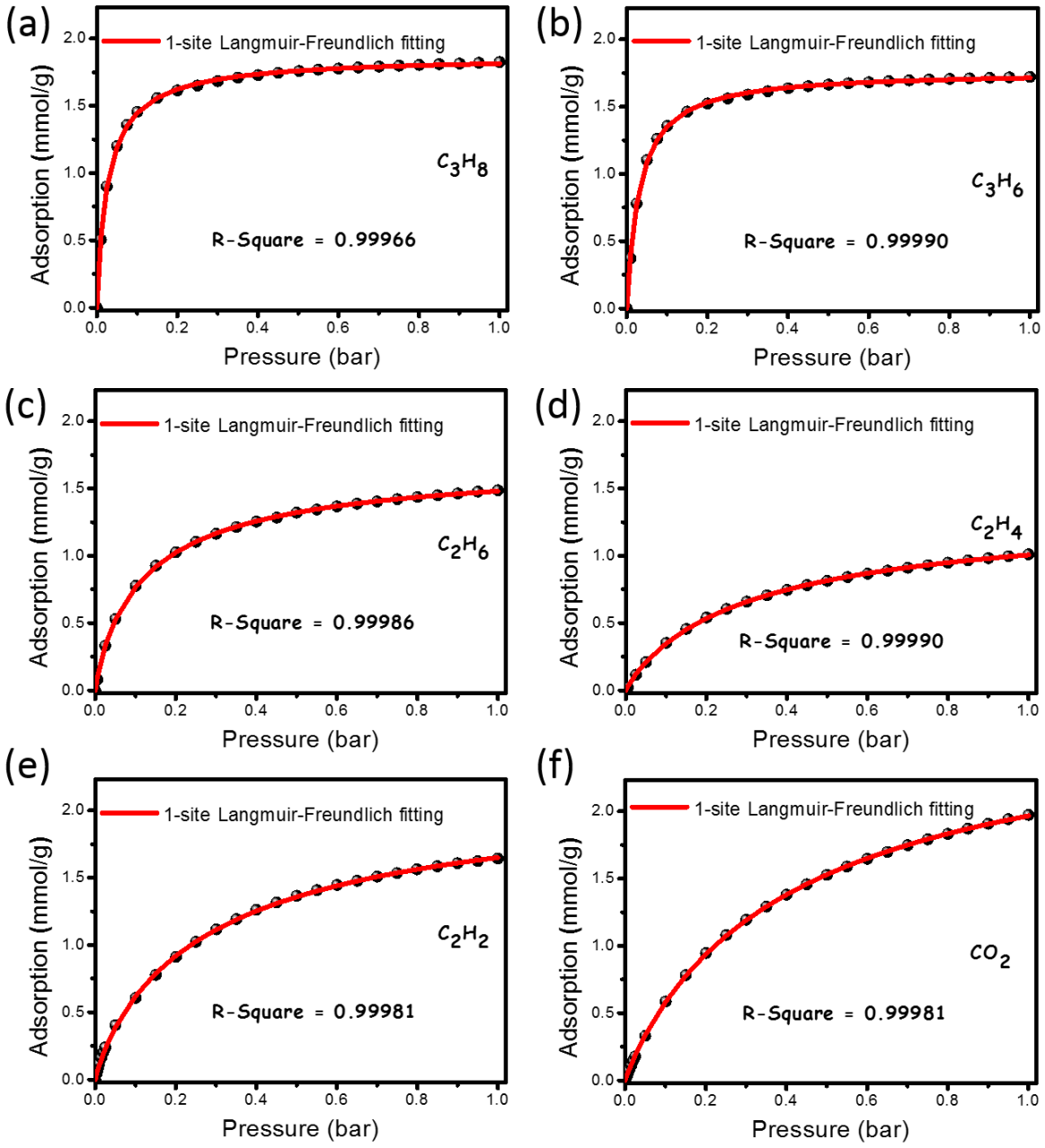

Fig. S14. C_3H_8, C_3H_6, C_2H_6, C_2H_4, C_2H_2, and CO_2 adsorption isotherms at 298 K for TYUT-12 with 1-site Langmuir–Freundlich model fits.

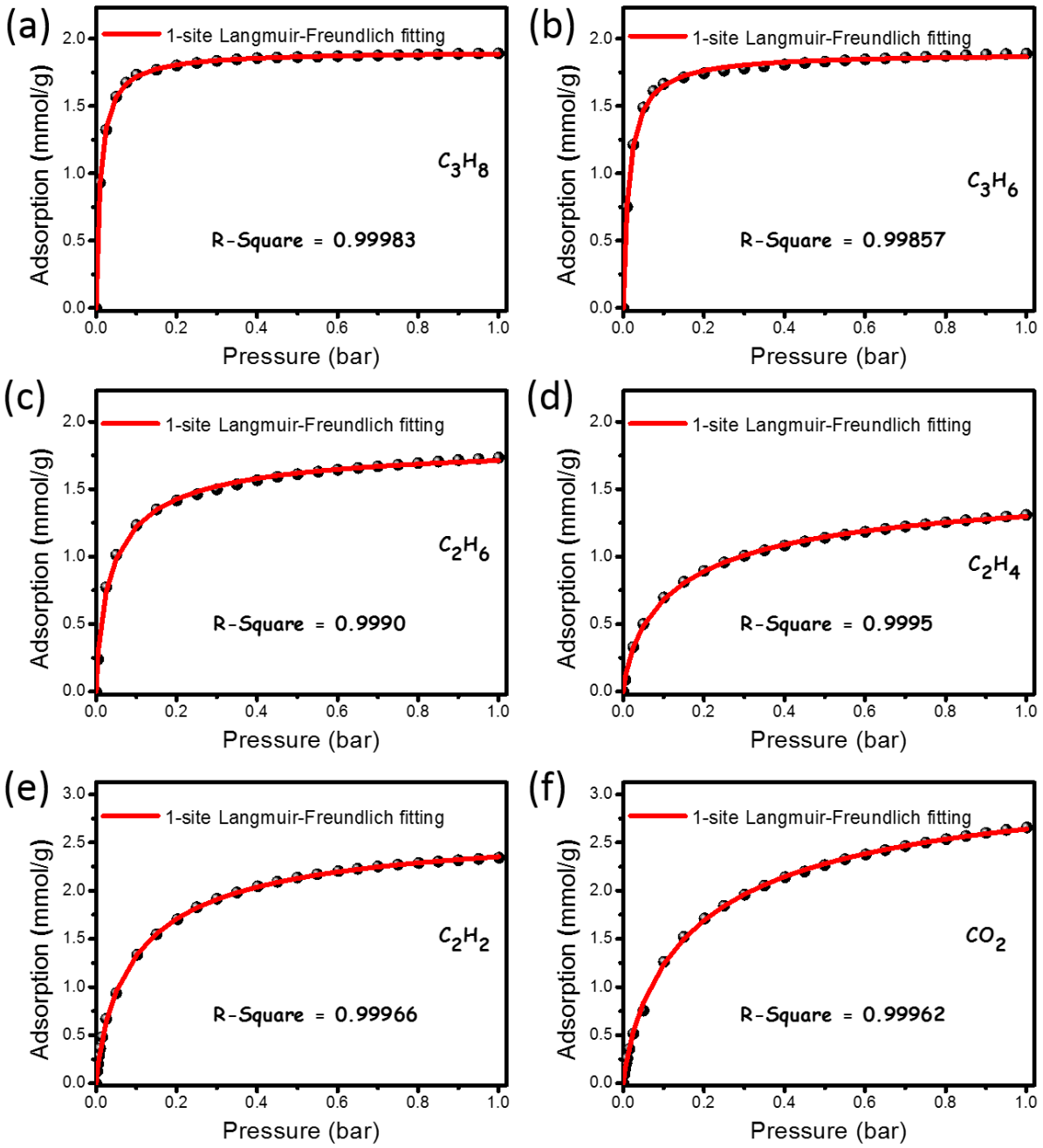

Fig. S15. C_3H_8, C_3H_6, C_2H_6, C_2H_4, C_2H_2, and CO_2 adsorption isotherms at 273 K for TYUT-12 with 1-site Langmuir–Freundlich model fits.

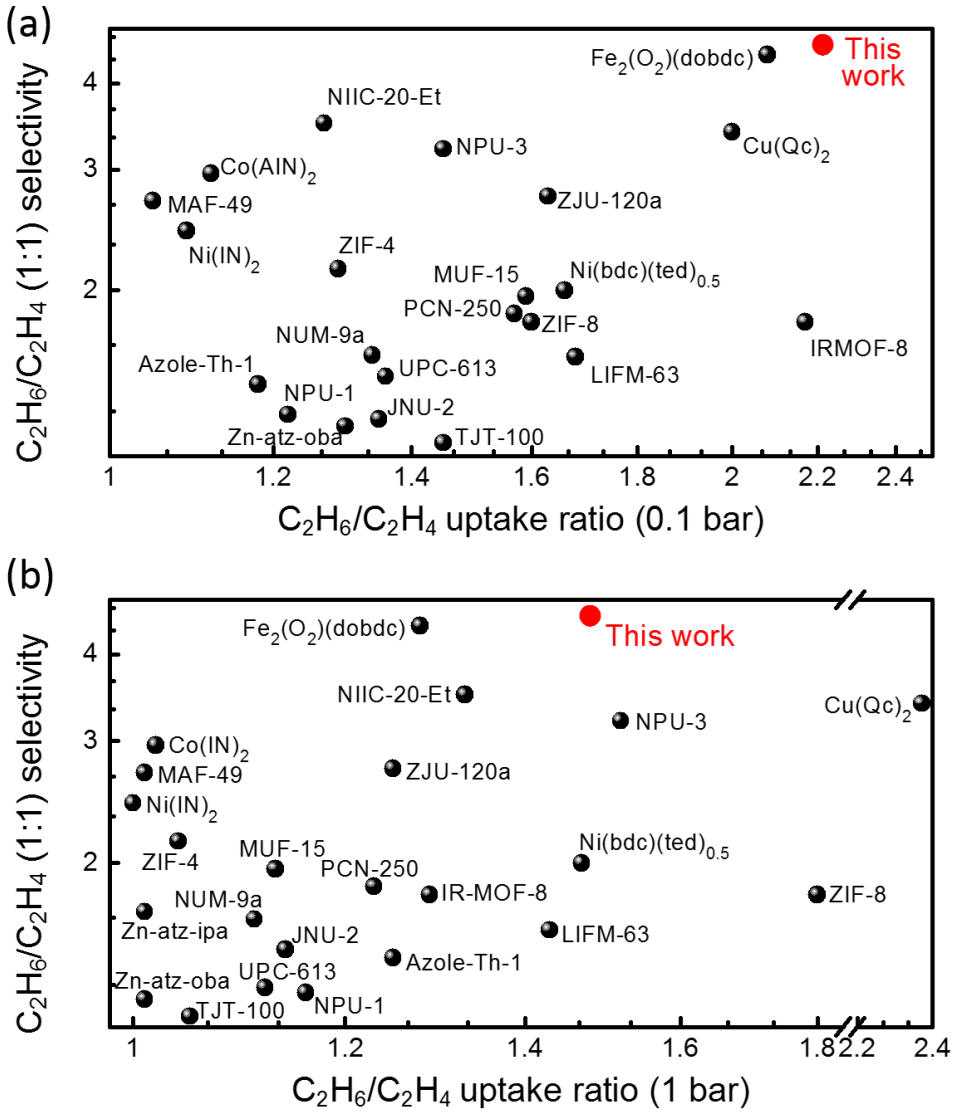

Fig. S16. The adsorption properties of TYUT-12 compare with the reported C_2H_6-selective adsorbent at 298 K.

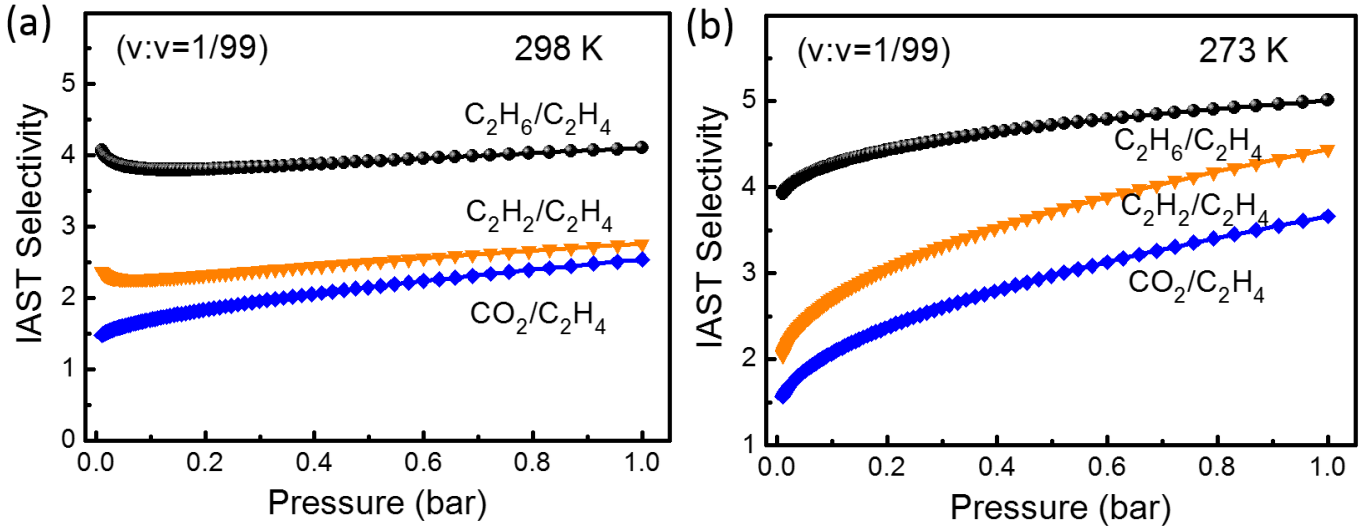

Fig. S17. IAST selectivities of C_2H_6/C_2H_4 (v/v, 1:99), C_2H_2/C_2H_4 (v/v, 1:99), CO_2/C_2H_4 (v/v, 1:99) mixtures for TYUT-12 at (a) 298 K and (b) 273 K.

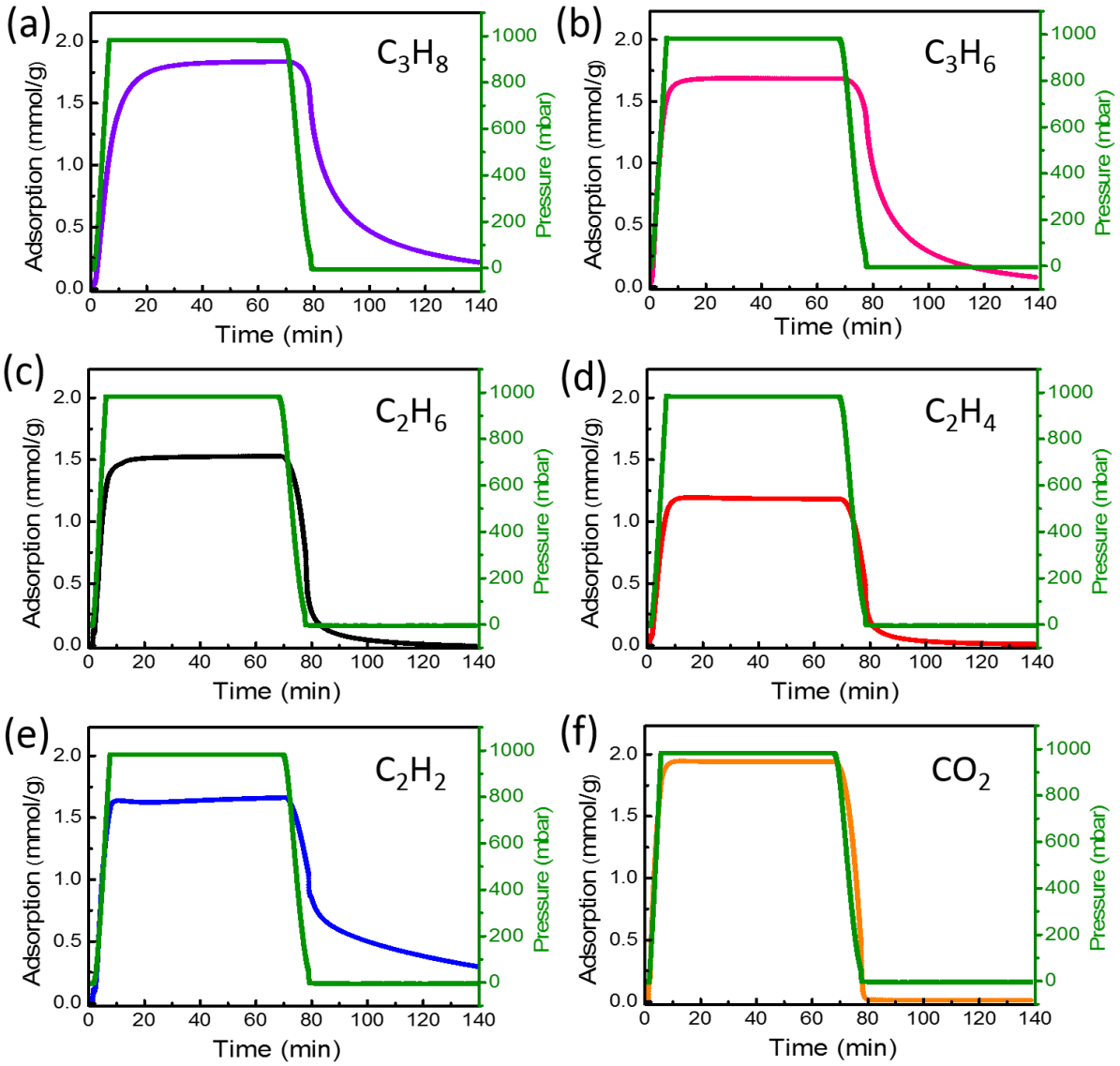

Fig. S18. Kinetic adsorption and desorption curves of C_3H_8, C_3H_6, C_2H_6, C_2H_4, C_2H_2, and CO_2 in TYUT-12 at 298 K.

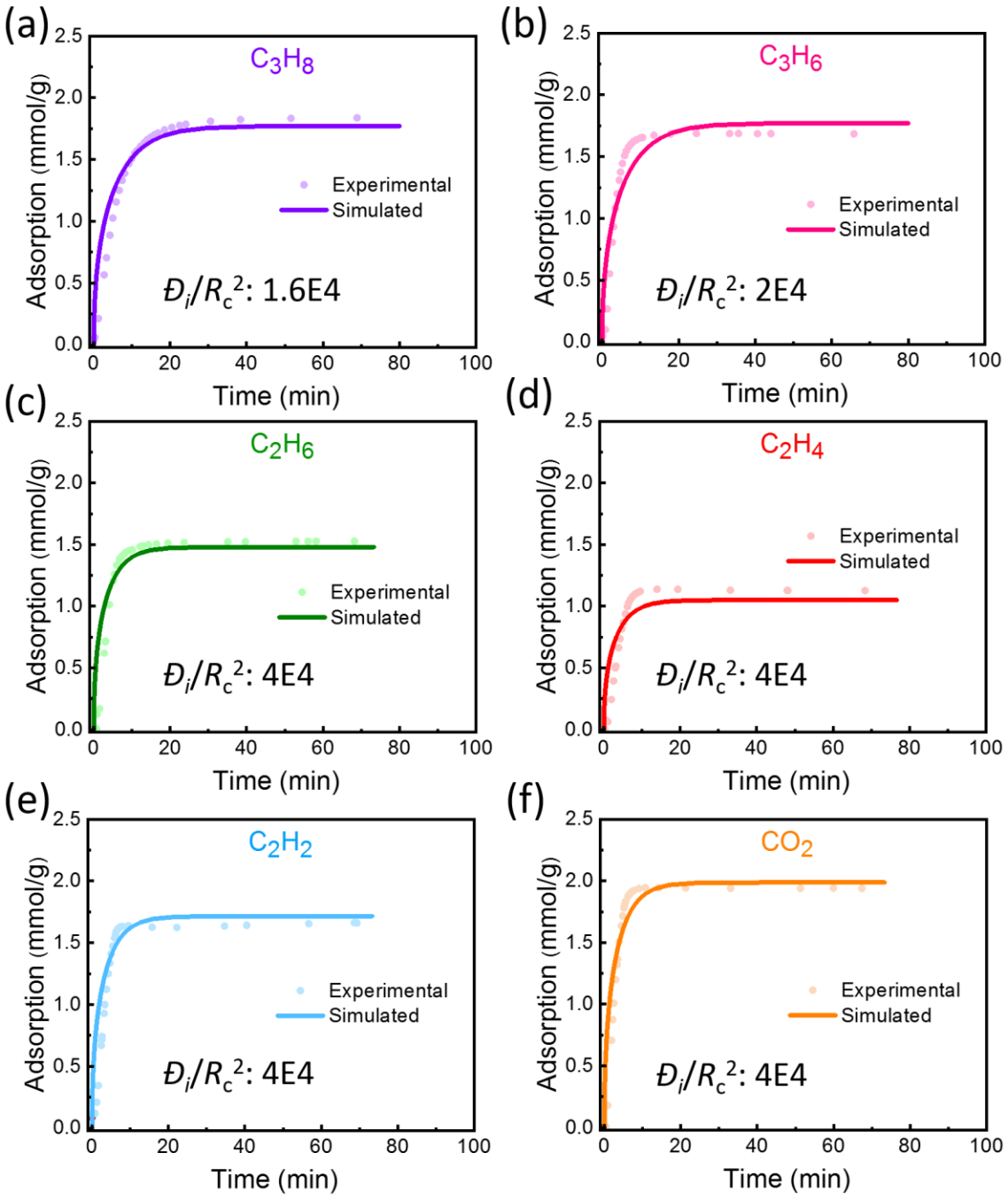

Fig. S19. The experimental and predicted kinetic adsorption curves of (a) C_3H_8, (b) C_3H_6, (c) C_2H_6, (d) C_2H_4, (e) C_2H_2, and (f) CO_2 in TYUT-12.

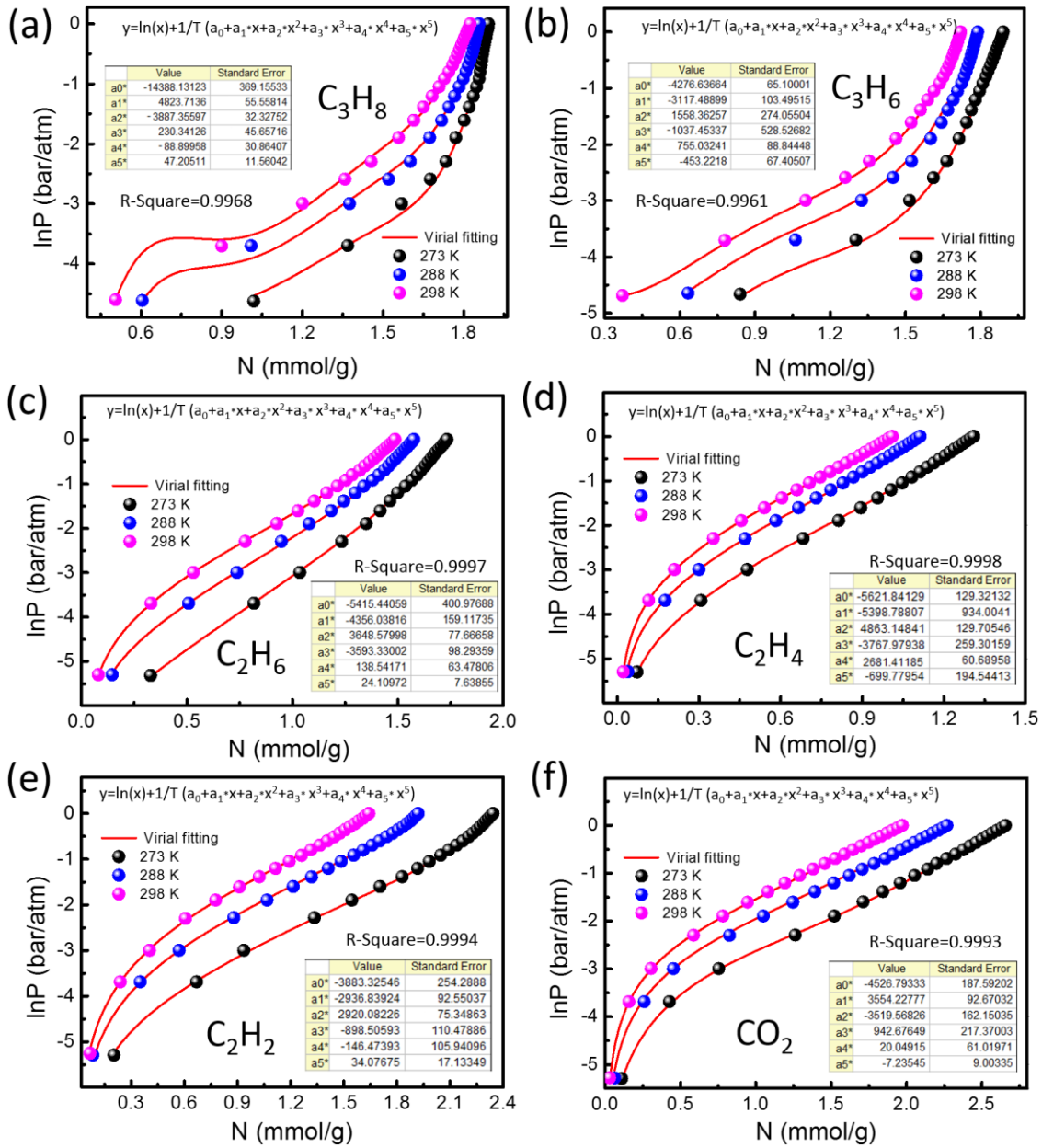

Fig. S20. Virial fitting of the (a) C_3H_8, (b) C_3H_6, (c) C_2H_6, (d) C_2H_4, (e) C_2H_2, and (f) CO_2 adsorption isotherms for TYUT-12.

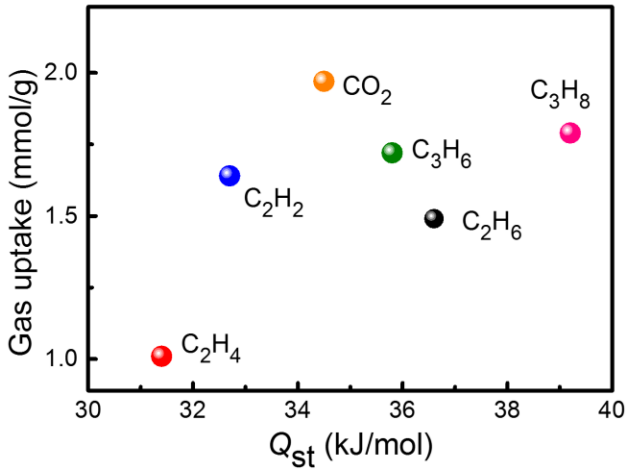

Fig. S21. The comparison of adsorption capacity and Q_{st} of C_3H_8, C_3H_6, C_2H_6, C_2H_4, C_2H_2, and CO_2 in TYUT-12 at 298 K.

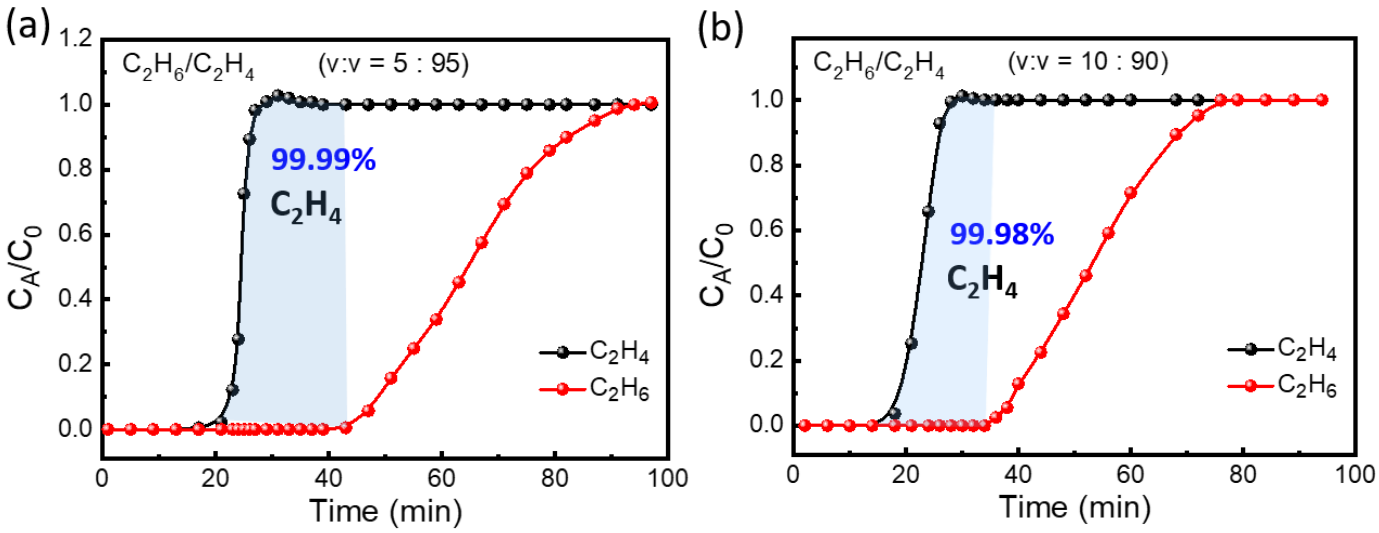

Fig. S22. Experimental breakthrough curves for C_2H_6/C_2H_4 (v/v = 5:95, 10:90) separation on TYUT-12 at 298 K and 1 bar.

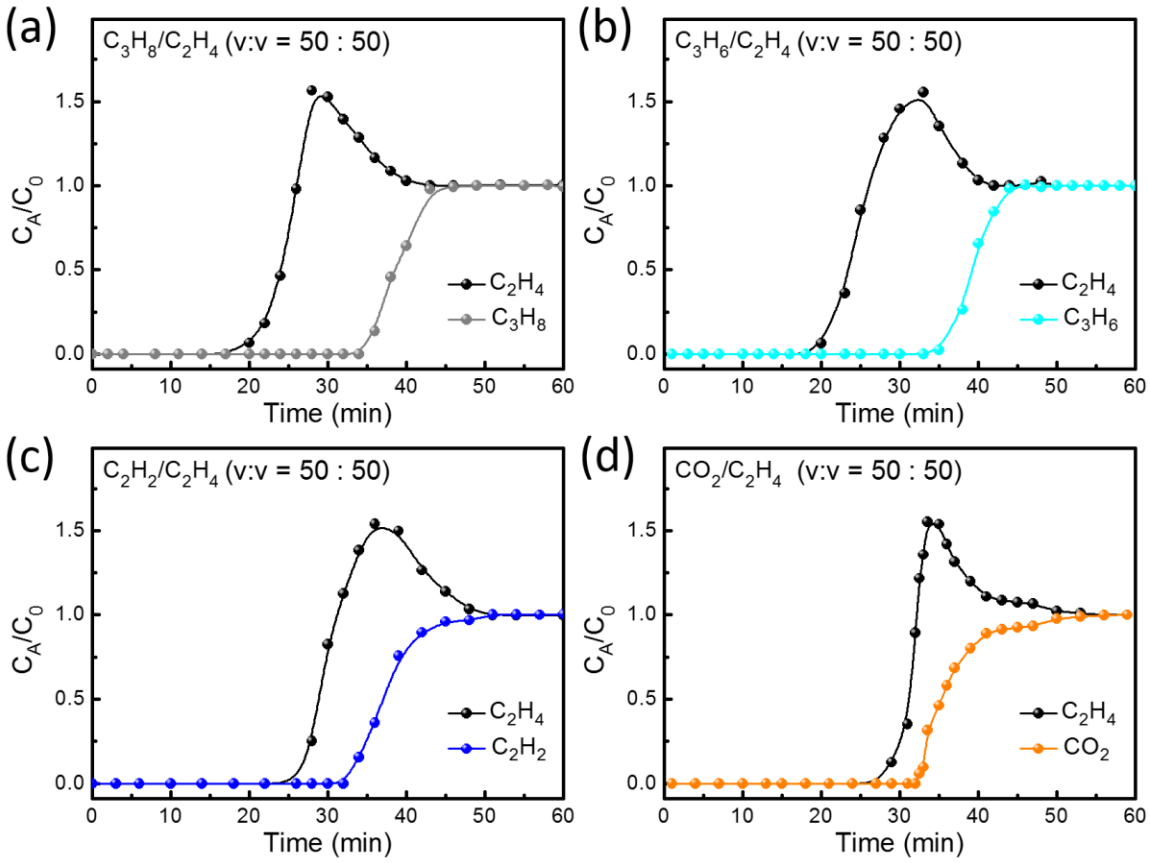

Fig. S23. Experimental breakthrough curves for equimolar C_3H_8/C_2H_4, C_3H_6/C_2H_4, C_2H_2/C_2H_4, and CO_2/C_2H_4 separation on TYUT-12 at 298 K and 1 bar.

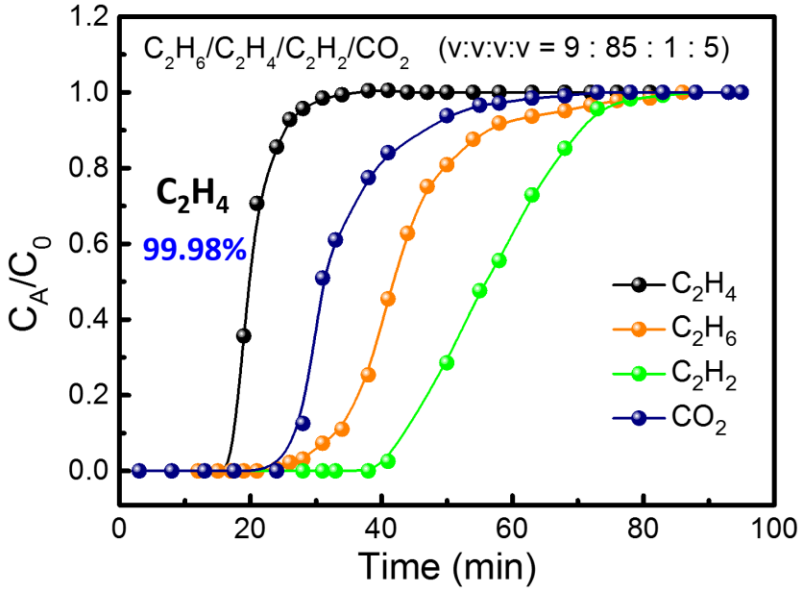

Fig. S24. Experimental breakthrough curves for quaternary $C_2H_6/C_2H_4/C_2H_2/CO_2$ (v/v/v/v, 9:85:1:5) mixtures separation on TYUT-12 at 298 K and 1 bar.

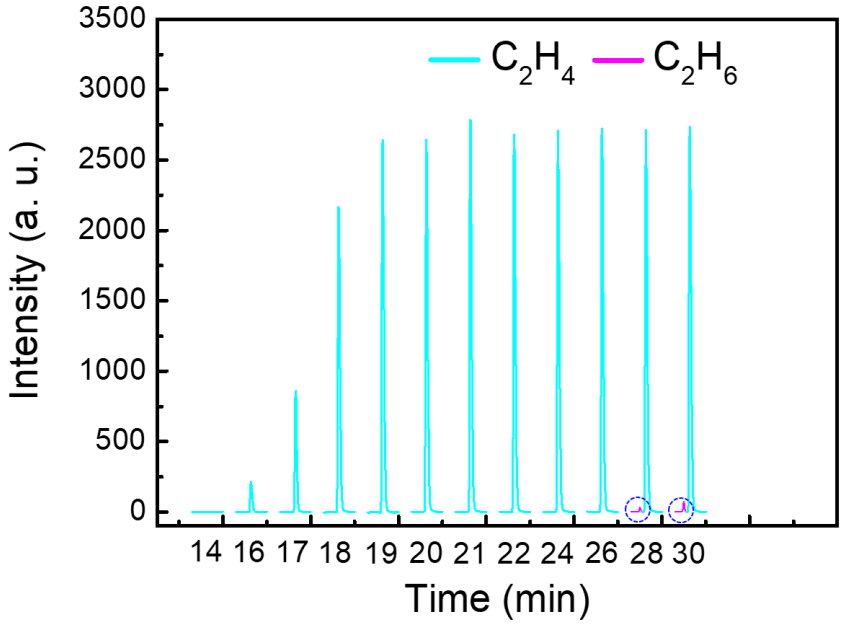

Fig. S25. The GC chromatogram signals during the breakthrough process ($C_2H_6/C_2H_4/C_2H_2/CO_2$, v/v/v/v, 9:89:1:1) in TYUT-12 at 298 K and 1 bar.

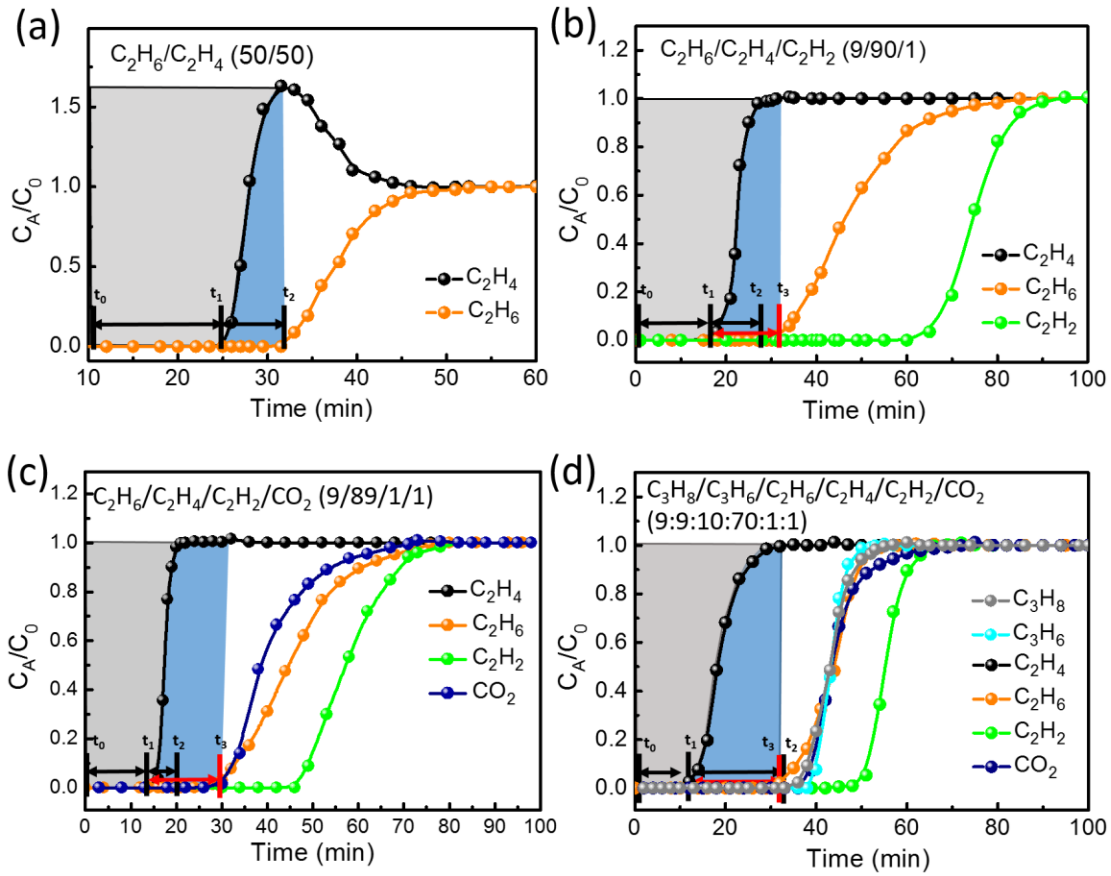

Fig. S26. The C_2H_4 capture amount and productivity calculation in the breakthrough process of TYUT-12 at 298 K and 1 bar.

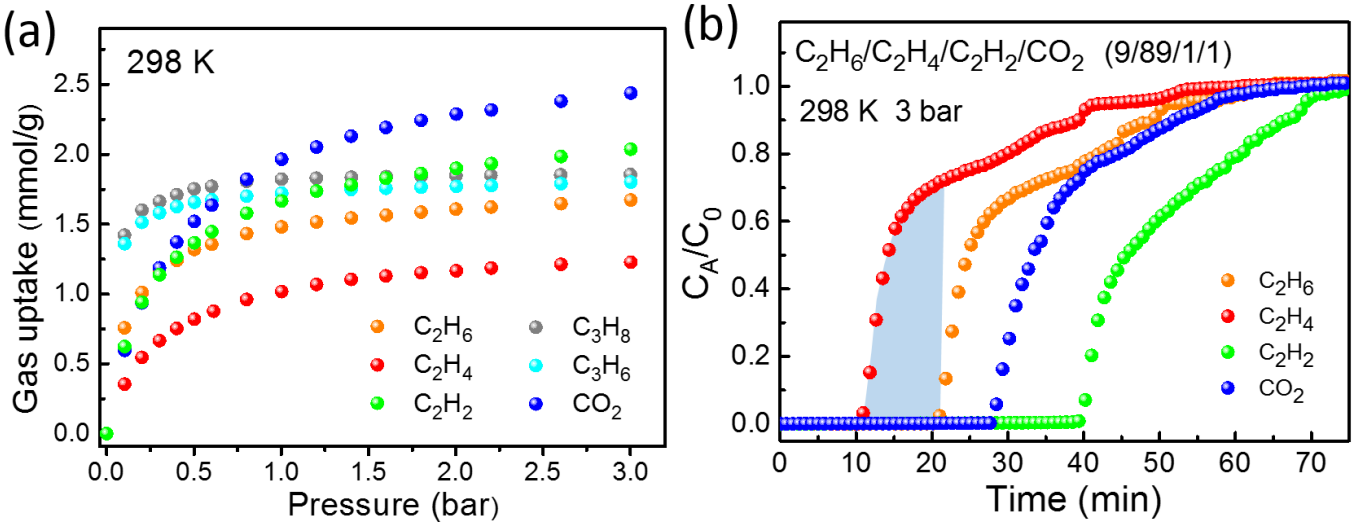

Fig. S27. (a) Single-component gas adsorption isotherms of C_3H_8, C_3H_6, C_2H_6, C_2H_4, C_2H_2, and CO_2 on TYUT-12 at 298 from 0 to 3 bar. (b) Experimental breakthrough curves for quaternary $C_2H_6/C_2H_4/C_2H_2/CO_2$ (v/v/v/v, 9:89:1:1) mixtures separation on TYUT-12 at 298 K and 3 bar.

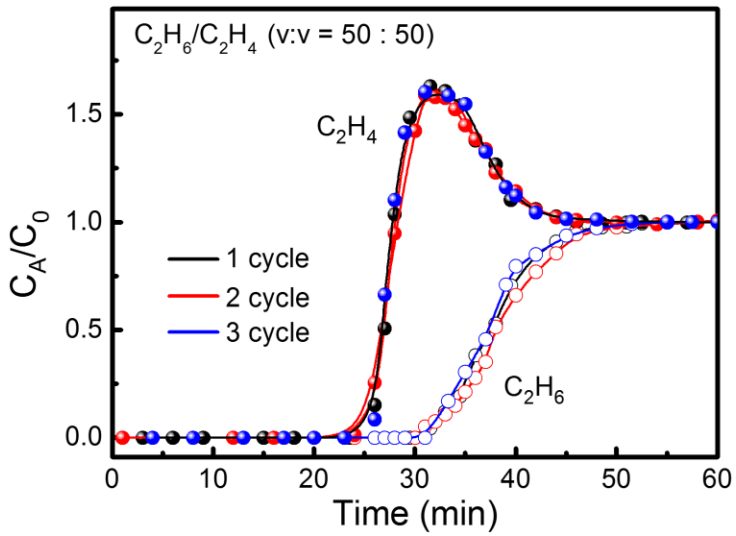

Fig. S28. Three cycle breakthrough curves for C_2H_6/C_2H_4 (v/v, 50:50) mixtures separation on TYUT-12 at 298 K and 1 bar.

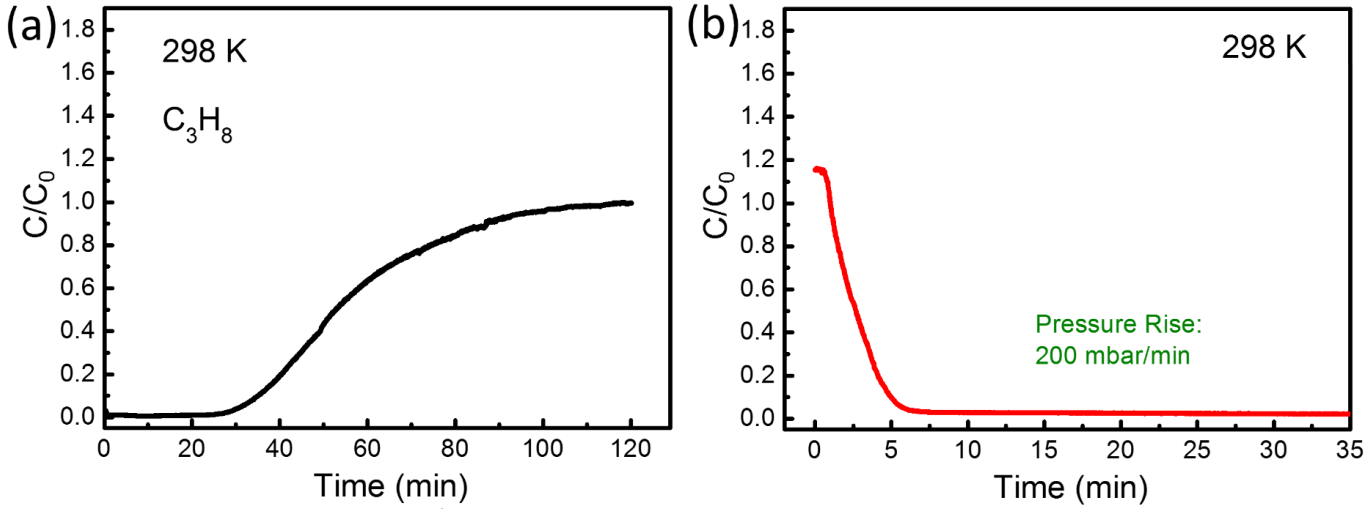

Fig. S29. (a) Breakthrough (1 mL·min^{-1}) and (b) regeneration curves of single-component C_3H_8 on TYUT-12 at 298 K and 1 bar.

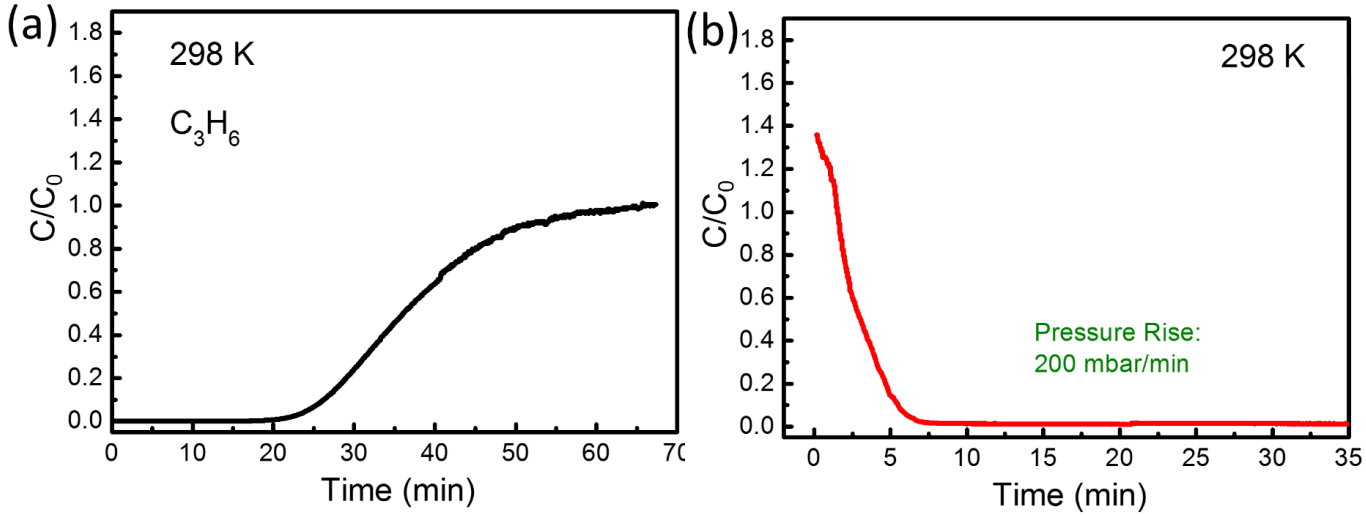

Fig. S30. (a) Breakthrough (1 mL·min^{-1}) and (b) regeneration curves of single-component C_3H_6 on TYUT-12 at 298 K and 1 bar.

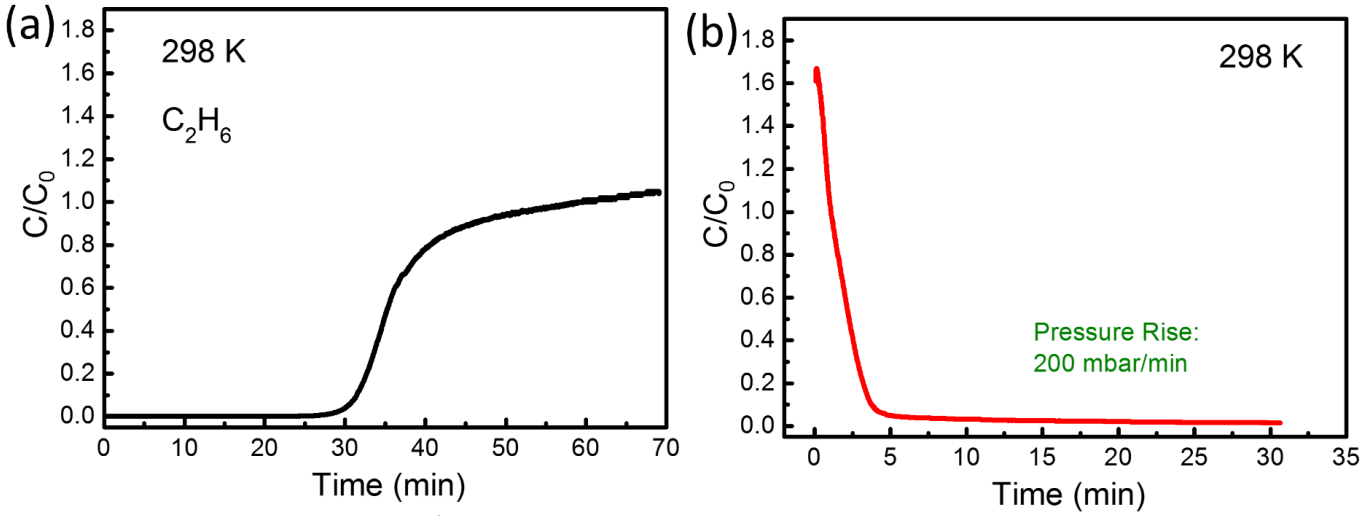

Fig. S31. (a) Breakthrough (1 mL·min^{-1}) and (b) regeneration curves of single-component C_2H_6 on TYUT-12 at 298 K and 1 bar.

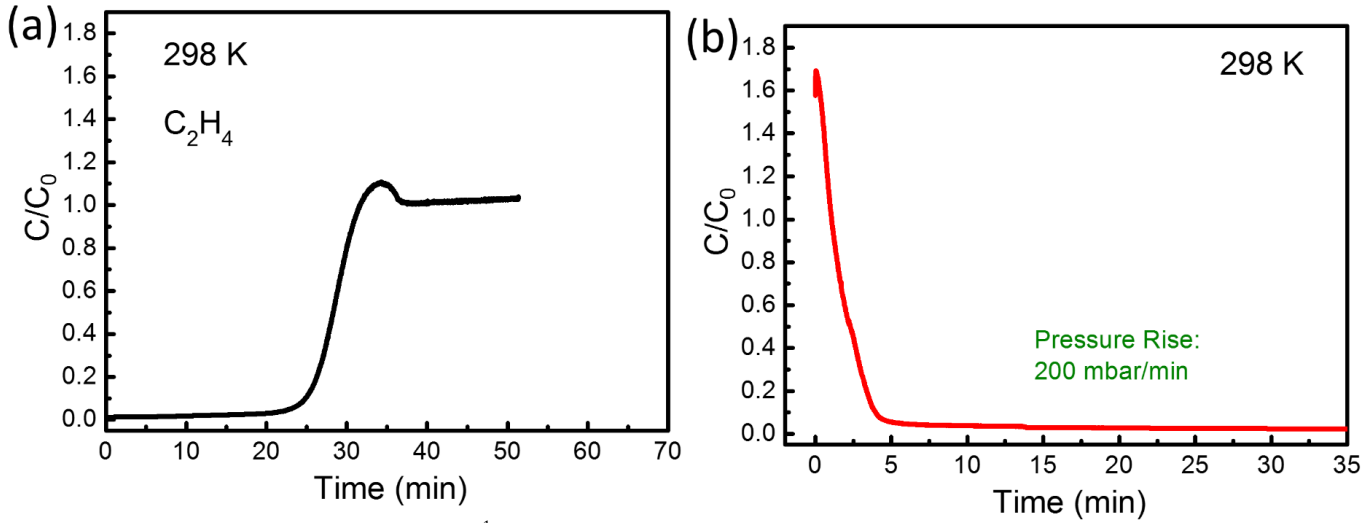

Fig. S32. (a) Breakthrough (1 mL·min^{-1}) and (b) regeneration curves of single-component C_2H_4 on TYUT-12 at 298 K.

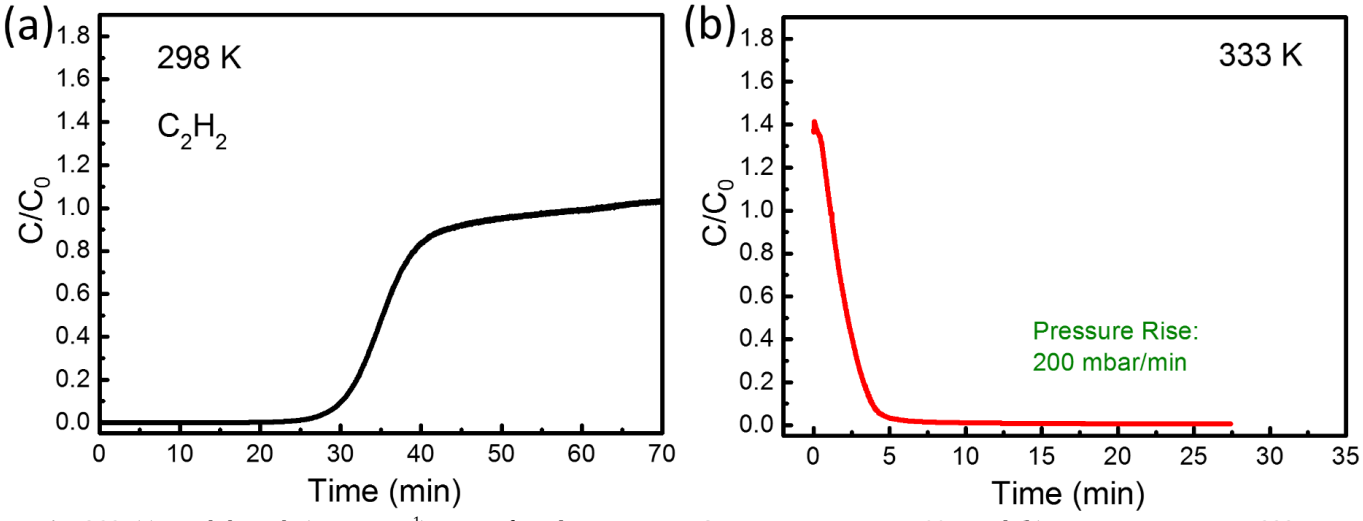

Fig. S33. (a) Breakthrough (1 mL·min^{-1}) curve of single-component C_2H_2 on TYUT-12 at 298 K and (b) regeneration curve at 333 K.

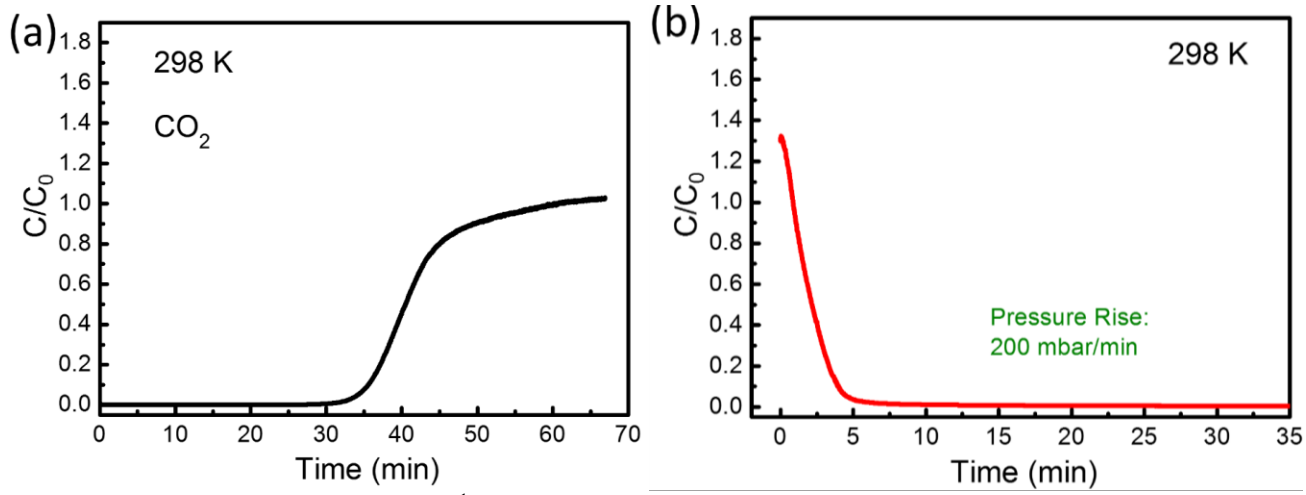

Fig. S34. (a) Breakthrough (1 mL·min^{-1}) and (b) regeneration curves of single-component CO_2 on TYUT-12 at 298 K.

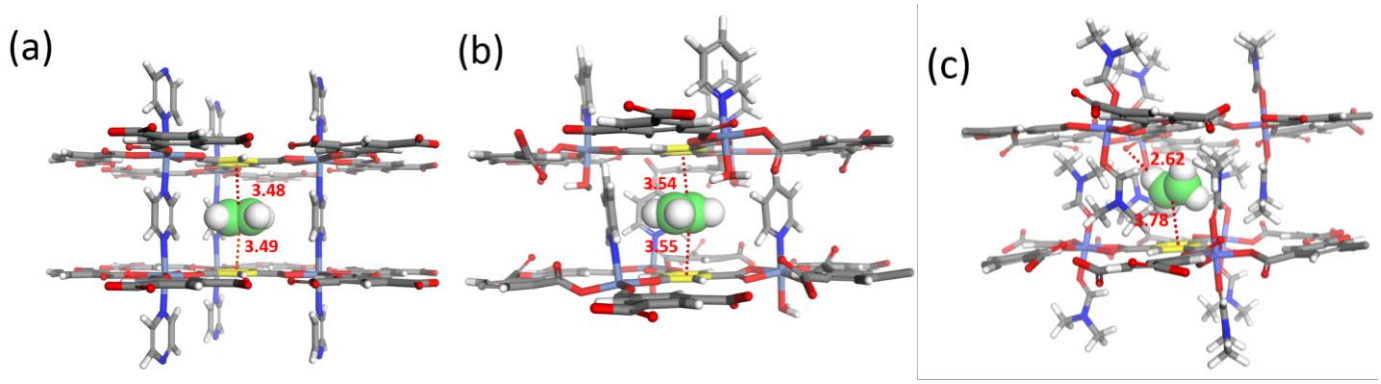

Fig. S35. Preferential adsorption sites in (a) TYUT-10, (b) TYUT-11, and (c) TYUT-13 of C_2H_4 as obtained from DFT calculations (color code: Ni, cyan; C, gray; H, white; O, red; N, blue).

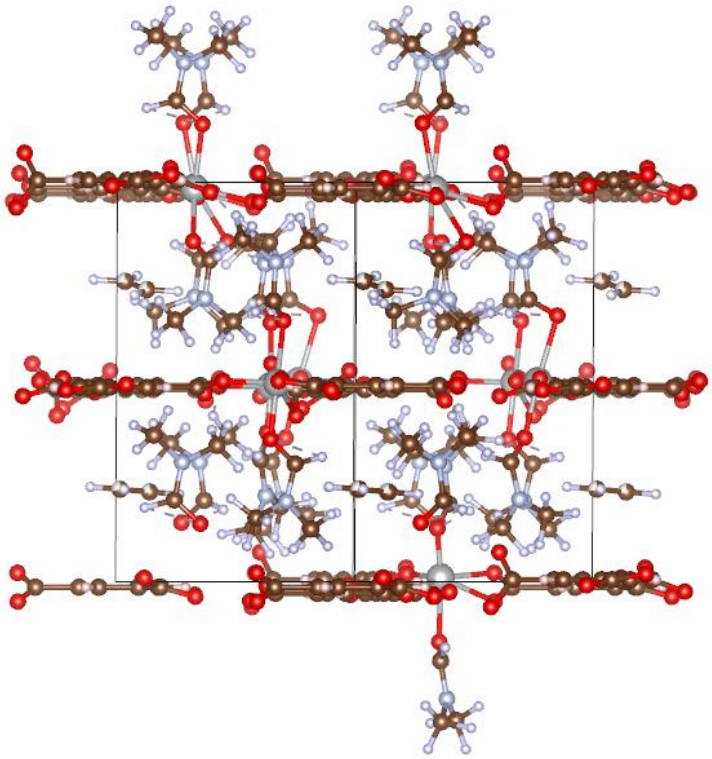

Fig. S36. The *P*1 structural model for the structure refinement.

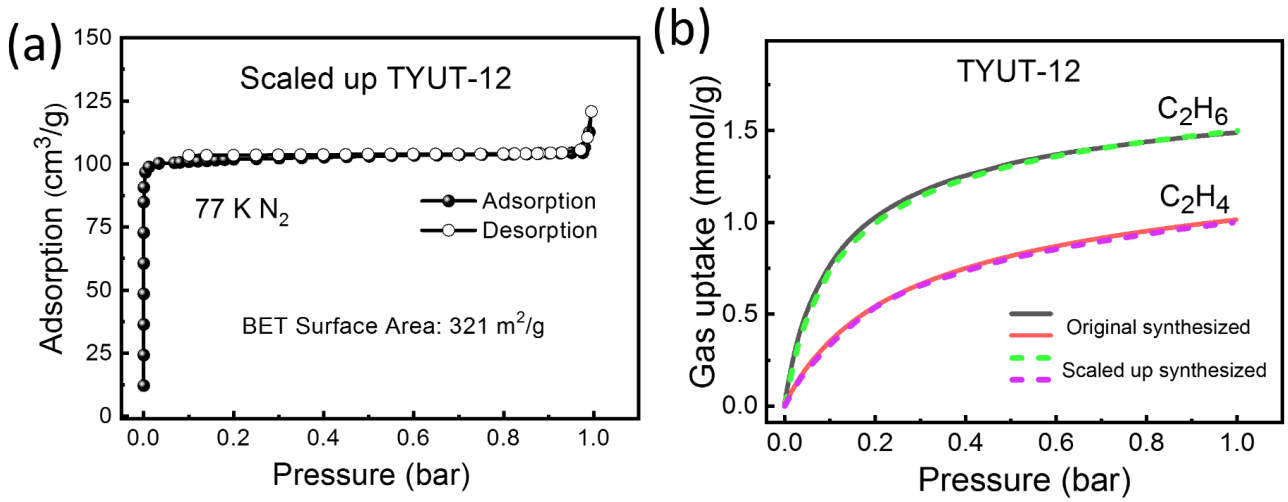

Fig. S37. The BET specific surface area and C_2H_6, C_2H_4 adsorption performance of the TYUT-12 sample prepared by scaled up method.

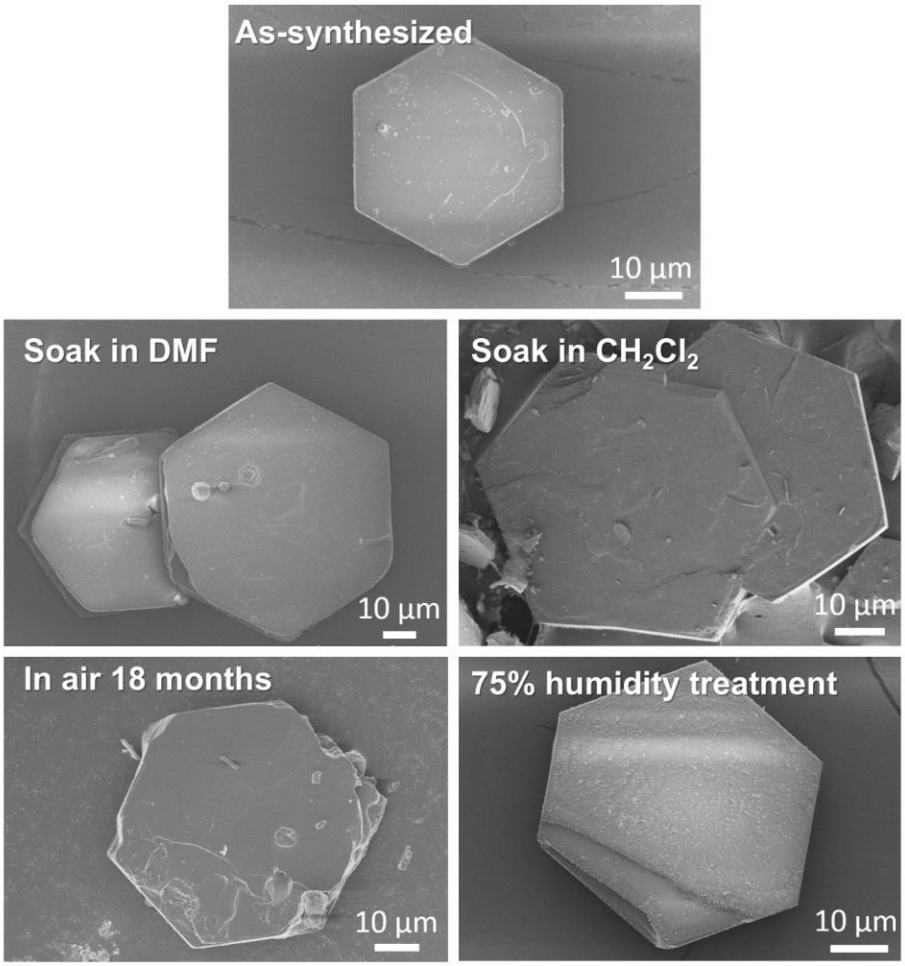

Fig. S38. SEM morphologies of TYUT-12 after treatment under different conditions.

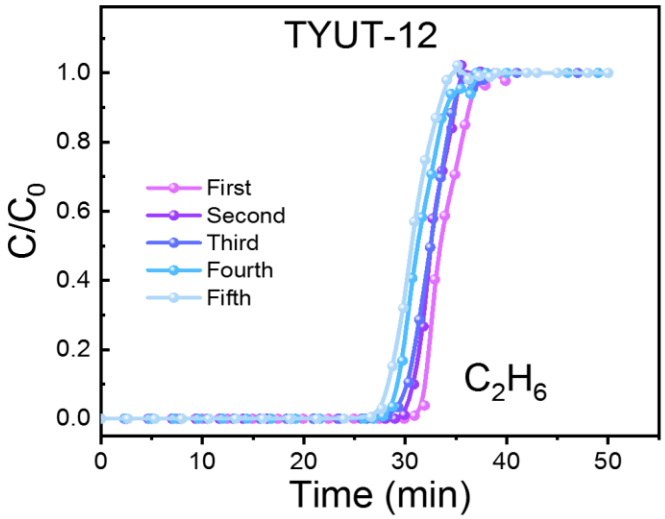

Fig. S39. Five cycles of C_2H_6 breakthrough (298 K, 1 mL·min^{-1}) under 75% humidity from TYUT-12.

Table S1
Crystallographic data of TYUT-11 and TYUT-13.

Compounds	TYUT-11	TYUT-13
CCDC	2110177	2115139
Empirical formula	$Ni_{1.5}C_{18.5}H_{9.5}O_{11}N$	$Co_3C_{45}H_{51}O_{24}N_6$
Formula weight	509.84	1236.71
Temperature (K)	193	296
Crystal system	trigonal	monoclinic
Space group	*P*3	$P2_{1/n}$
a (Å)	16.5911(2)	16.6303(18)
b (Å)	16.5911(2)	14.1470(15)
c (Å)	13.9691(3)	28.740(3)
α (°)	90	90
β (°)	90	90.003(4)
γ (°)	120	90
Volume (Å^3)	3330.04(11)	6761.7(12)
Z	*3*	4
D_c (g·cm^{-3})	0.763	1.215
μ (mm^{-1})	3.681	0.797
F(000)	772	2544
Radiation	Ga Kα (*λ* =1.34139 Å)	Mo Kα (λ = 0.71073 Å)
GOF	1.027	1.093
Final *R* indexes [$I \geq 2\sigma(I)$][a]	R_1 = 0.0793, wR_2 = 0.2121	R_1 = 0.0925, wR_2 = 0.3931
Final *R* indexes [all data][a]	R_1 = 0.0819, wR_2 = 0.2160	R_1 = 0.2539, wR_2 = 0.2602

[a] $R_1 = \sum\left||F_o|-|F_c|\right| / \sum|F_o|$; $wR_2 = \left[\sum w\left(|F_o|^2-|F_c|^2\right)^2 / \sum w\left(F_o^2\right)^2\right]^{1/2}$

Table S2
Crystallographic data of TYUT-12 and TYUT-12 $0.72C_2D_4$.

Crystallographic data	TYUT-12	TYUT-12·$0.72C_2D_4$
Empirical formula	$Ni_3C_{45}H_{51}O_{24}N_6$	$Ni_3C_{46.44}D_{53.88}O_{24}N_6$
Formula weight	1235.07	1301.37
a (Å)	16.609	16.660
b (Å)	16.609	16.628
c (Å)	14.325	13.8901
α (°)	90	90.050
β (°)	90	89.652
γ (°)	120	120.165
Volume ($Å^3$)	3244.25	3326.64
D_c ($g·cm^{-3}$)	1.1995	1.2992

Table S3
Langmuir–Freundlich fit parameters for C_2H_6 and C_2H_4 in TYUT-10, TYUT-11, and TYUT-13.

Material	Adsorbate	q_{sat} ($mol·kg^{-1}$)	b_0 (Pa^{-v})	*v*
TYUT-10	C_2H_6	4.25	1.458×10^{-4}	1.02
	C_2H_4	4.41	1.261×10^{-4}	0.98
TYUT-11	C_2H_6	1.99	1.769×10^{-4}	0.84
	C_2H_4	2.00	9.784×10^{-5}	0.87
TYUT-13	C_2H_6	0.94	2.423×10^{-4}	0.82
	C_2H_4	1.18	7.404×10^{-5}	0.90

Table S4
1-site Langmuir–Freundlich fits for C_3H_8, C_3H_6, C_2H_6, C_2H_4, C_2H_2, and CO_2 in TYUT-12.

Adsorbate	q_{sat} ($mol·kg^{-1}$)	b_0 (Pa^{-v})	*E* ($kJ·mol^{-1}$)	*v*
C_3H_8	1.90	1.109×10^{-8}	27.2	0.920
C_3H_6	1.86	5.489×10^{-9}	28.0	0.935
C_2H_6	1.75	1.685×10^{-10}	35.2	0.870
C_2H_4	1.45	2.053×10^{-10}	30.7	0.940
C_2H_2	2.75	2.417×10^{-10}	33.6	0.790
CO_2	3.04	1.842×10^{-10}	30.6	0.930

Table S5
Pore characterizes and adsorption properties of TYUT-10, TYUT-11, TYUT-12, and TYUT-13 materials.

Materials	S_{BET} ($m^2·g^{-1}$)	Pore size distribution[c] (nm)	Uptake at 298 K and 1 bar ($mmol·g^{-1}$)						C_2H_6/C_2H_4	
			C_3H_8	C_3H_6	C_2H_6	C_2H_4	C_2H_2	CO_2	Uptake ratio (1 bar)	IAST selectivity (50:50)
TYUT-10	867[a]	0.74	4.28	4.33	4.09	4.02	4.61	5.10	1.02	1.37
TYUT-11	275[a]	0.64	2.26	2.38	1.48	1.39	1.70	2.00	1.07	1.55
TYUT-12	327[a]	0.59	1.80	1.74	1.49	1.01	1.64	1.97	1.48	4.56
TYUT-13	61[b]	0.56	0.03	0.08	0.72	0.83	1.02	1.07	0.87	1.04

[a] N_2 adsorption (77 K).
[b] CO_2 adsorption (196 K).
[c] Calculated by Horváth–Kawazoe equation.

Table S6
Diffusional time constants of C_3H_8, C_3H_6, C_2H_6, C_2H_4, C_2H_2, and CO_2 in TYUT-12.

Adsorbate	C_3H_8	C_3H_6	C_2H_6	C_2H_4	C_2H_2	CO_2
D_i/R_c^2 (s^{-1})	1.6×10^{-4}	2×10^{-4}	4×10^{-4}	4×10^{-4}	4×10^{-4}	4×10^{-4}

Table S7
The adsorption energy (E_{ads}) of C_3H_8, C_3H_6, C_2H_6, C_2H_4, C_2H_2, and CO_2 molecule in the pore cavities of TYUT-12.

Adsorbate	C_3H_8	C_3H_6	C_2H_6	C_2H_4	C_2H_2	CO_2
E_{ads} ($kJ \cdot mol^{-1}$)	−59.9	−57.3	−50.4	−34.2	−48.9	−55.5

Table S8
Summary of adsorption capacities of C_3H_8, C_3H_6, C_2H_6, C_2H_4, C_2H_2, and CO_2 and in TYUT-12 and representative MOFs for multi-component hydrocarbons separation.

Materials	S_{BET} ($m^2 \cdot g^{-1}$)	Uptake at 298 K and 1 bar ($mmol \cdot g^{-1}$)						IAST selectivity (50:50)			Breakthrough selectivity (1:1)[d]	Ref.
		C_3H_8	C_3H_6	C_2H_6	C_2H_4	C_2H_2	CO_2	C_2H_6/C_2H_4	C_2H_2/C_2H_4	CO_2/C_2H_4	C_2H_6/C_2H_4	
MAF-49	—	—	—	1.73	1.70	—	1.52	2.7	—	—	1.31	15
TJT-100	890	—	—	3.66	3.39	4.46	—	1.2[c]	1.8	—	—	16
Zn-atz-ipa	650	—	—	1.81	1.80	1.99	1.90	1.7	—	—	—	17
Azloe-Th-1	983	—	—	4.47	3.62	3.66	—	1.46	—	—	1.13	18
ZJNU-115	1291	—	—	4.21	3.75	—	—	1.56	2.05	—	—	19
ZJNU-7	1180	—	—	4.13	3.80	5.04	—	1.56	2.31	—	—	20
MOF-525	3116	—	—	2.71	2.11	2.65	—	1.22	1.48	—	—	21
UPC-612	2017	—	—	3.58	2.79	3.01	—	1.4	1.09	—	—	21
NUM-9	—	—	—	2.48	2.37	2.28	—	1.61	1.49	—	1.05[e]	22
NPU-3	1834	—	—	3.33	2.19	2.54	—	3.21	1.32	—	—	23
NTU-67	380	—	—	—	1.41	3.27	2.04	—	8.1[c]	10.8	—	24
UiO-67-$(NH_2)_2$[a]	2815	—	—	3.05	2.13	2.09	—	1.7	2.1[c]	—	1.15	25
Zn(BDC)(H_2BPZ)	907	—	—	3.63	3.29	4.46	—	2.2	1.6	—	1.53	26
$CuTiF_6$-TPPY	685	—	—	2.82	2.42	3.62	—	2.12	5.47	—	1.38	27
MFM-520	313	2.02	2.33	1.93	2.36	3.09	—	—	9.6	—	—	28
Al-MOFM$_{15}$[b]	793	—	—	2.23	1.29	2.86	1.79	2.51	3.32	—	3.30	29
Zn-atz-oba	711	—	—	2.05	2.03	2.77	2.50	1.27	1.43	1.33	1.12	30
Al-PyDC	1134	—	—	4.20	3.44	8.24	—	1.9	4.3[c]	v	1.20	31
TYUT-12	327	1.80	1.74	1.49	1.01	1.64	1.97	4.56	2.76	2.54	1.40	This work

[a] Gas uptake and selectivity at 296 K.
[b] Gas uptake and selectivity at 293 K.
[c] Selectivity for 1/99 gas mixture.
[d] Due to differences in separation test conditions, this value is an estimate.
[e] Selectivity for 1/9 gas mixture.

References

[1] Gao C, Liu S, Xie L, Ren Y, Cao J, Sun C. Design and construction of a microporous metal–organic framework based on the pillared-layer motif. CrystEngComm 2007;9(7):545–7.
[2] VandeVondele J, Krack M, Mohamed F, Parrinello M, Chassaing T, Hutter J. Quickstep: fast and accurate density functional calculations using a mixed Gaussian and plane waves approach. Comput Phys Commun 2005;167(2):103–28.
[3] VandeVondele J, Hutter J. Gaussian basis sets for accurate calculations on molecular systems in gas and condensed phases. J Chem Phys 2007;127:114105.
[4] Perdew JP, Burke K, Ernzerhof M. Generalized gradient approximation made simple. Phys Rev Lett 1996;77(18):3865–8.
[5] Goedecker S, Teter M, Hutter J. Separable dual-space Gaussian pseudopotentials. Phys Rev B 1996;54(3):1703–10.
[6] Hartwigsen C, Goedecker S, Hutter J. Relativistic separable dual-space Gaussian pseudopotentials from H to Rn. Phys Rev B 1998;58(7):3641–62.
[7] Krack M, Parrinello M. All-electron *ab-initio* molecular dynamics. Phys Chem Chem Phys 2000;2(10):2105–12.
[8] Grimme S, Antony J, Ehrlich S, Krieg H. A consistent and accurate *ab initio* parametrization of density functional dispersion correction (DFT-D) for the 94 elements H–Pu. J Chem Phys 2010;132(15):154104.

[9] Myers AL, Prausnitz JM. Thermodynamics of mixed-gas adsorption. AIChE J 1965;11(1):121–7.
[10] Krishna R. Describing the diffusion of guest molecules inside porous structures. J Phys Chem C 2009;113(46):19756–81.
[11] Krishna R. Diffusion in porous crystalline materials. Chem Soc Rev 2012;41(8):3099–118.
[12] Krishna R. Highlighting the influence of thermodynamic coupling on kinetic separations with microporous crystalline materials. ACS Omega 2019;4(2):3409–19.
[13] Krishna R. Metrics for evaluation and screening of metal–organic frameworks for applications in mixture separations. ACS Omega 2020;5(28):16987−7004.
[14] Lin RB, Li L, Zhou HL, Wu H, He C, Li S, et al. Molecular sieving of ethylene from ethane using a rigid metal–organic framework. Nat Mater 2018;17(12):1128–33.
[15] Liao PQ, Zhang WX, Zhang JP, Chen XM. Efficient purification of ethene by an ethane-trapping metal–organic framework. Nat Commun 2015;6(1):8697.
[16] Hao HG, Zhao YF, Chen DM, Yu JM, Tan K, Ma S, et al. Simultaneous trapping of C_2H_2 and C_2H_6 from a ternary mixture of $C_2H_2/C_2H_4/C_2H_6$ in a robust metal–organic framework for the purification of C_2H_4. Angew Chem Int Ed Engl 2018;57(49):16067–71.
[17] Chen KJ, Madden DG, Mukherjee S, Pham T, Forrest KA, Kumar A, et al. Synergistic sorbent separation for one-step ethylene purification from a four-component mixture. Science 2019;366(6462):241–6.
[18] Xu Z, Xiong X, Xiong J, Krishna R, Li L, Fan Y, et al. A robust Th-azole framework for highly efficient purification of C_2H_4 from a $C_2H_4/C_2H_2/C_2H_6$ mixture. Nat Commun 2020;11(1):3163.
[19] Fan L, Zhou P, Wang X, Yue L, Li L, He Y. Rational construction and performance regulation of an In(III)–tetraisophthalate framework for one-step adsorption-phase purification of C_2H_4 from C_2 Hydrocarbons. Inorg Chem 2021;60(14):10819−29.
[20] Jiang Z, Fan L, Zhou P, Xu T, Hu S, Chen J, et al. An aromatic-rich cage-based MOF with inorganic chloride ions decorating the pore surface displaying the preferential adsorption of C_2H_2 and C_2H_6 over C_2H_4. Inorg Chem Front 2021;8(5):1243–52.
[21] Wang Y, Hao C, Fan W, Fu M, Wang X, Wang Z, et al. One-step ethylene purification from an acetylene/ethylene/ethane ternary mixture by cyclopentadiene cobalt-functionalized metal–organic frameworks. Angew Chem Int Ed Engl 2021;60(20):11350–8.
[22] Yang SQ, Sun FZ, Liu P, Li L, Krishna R, Zhang YH, et al. Efficient purification of ethylene from C_2 hydrocarbons with an C_2H_6/C_2H_2-selective metal–organic framework. ACS Appl Mater Interfaces 2021;13(1):962–9.
[23] Zhu B, Cao JW, Mukherjee S, Pham T, Zhang T, Wang T, et al. Pore engineering for one-step ethylene purification from a three-component hydrocarbon mixture. J Am Chem Soc 2021;143(3):1485–92.
[24] Dong Q, Huang Y, Hyeon-Deuk K, Chang IY, Wan J, Chen C, et al. Shape- and size-dependent kinetic ethylene sieving from a ternary mixture by a trap-and-flow channel crystal. Adv Funct Mater 2022;32(38):2203745.
[25] Gu XW, Wang JX, Wu E, Wu H, Zhou W, Qian G, et al. Immobilization of Lewis basic sites into a stable ethane-selective MOF enabling one-step separation of ethylene from a ternary mixture. J Am Chem Soc 2022;144(6):2614–23.
[26] Wang GD, Li YZ, Shi WJ, Hou L, Wang YY, Zhu Z. One-step C_2H_4 purification from ternary $C_2H_6/C_2H_4/C_2H_2$ mixtures by a robust metal–organic framework with customized pore environment. Angew Chem Int Ed 2022;61(28):e202205427.
[27] Zhang P, Zhong Y, Zhang Y, Zhu Z, Liu Y, Su Y, et al. Synergistic binding sites in a hybrid ultramicroporous material for one-step ethylene purification from ternary C_2 hydrocarbon mixtures. Sci Adv 2022;8(23):eabn9231.
[28] Li J, Han X, Kang X, Chen Y, Xu S, Smith GL, et al. Purification of propylene and ethylene by a robust metal–organic framework mediated by host–guest interactions. Angew Chem Int Ed Engl 2021;60(28):15541–7.
[29] Laha S, Dwarkanath N, Sharma A, Rambabu D, Balasubramanian S, Maji TK. Tailoring a robust Al-MOF for trapping C_2H_6 and C_2H_2 towards efficient C_2H_4 purification from quaternary mixtures. Chem Sci 2022;13(24):7172–80.
[30] Cao JW, Mukherjee S, Pham T, Wang Y, Wang T, Zhang T, et al. One-step ethylene production from a four-component gas mixture by a single physisorbent. Nat Commun 2021;12(1):6507.
[31] Wu E, Gu XW, Liu D, Zhang X, Wu H, Zhou W, et al. Incorporation of multiple supramolecular binding sites into a robust MOF for benchmark one-step ethylene purification. Nat Commun 2023;14(1):6146.